Pseudouridine selects RNAs for extracellular transport

Alessandro Scacchetti[1†], Emily J. Shields[1], Lauren N. Reich[1], John F. Doherty[1], Julia A. Tasca[1], Grace E. Lee[2,3], Richard Lauman[1], Natali L. Chanaday[4], Benjamin A. Garcia[5], Colin C. Conine[2,3], and Roberto Bonasio[1†]

[1]Epigenetics Institute and Department of Cell and Developmental Biology; University of Pennsylvania Perelman School of Medicine, Philadelphia, Pennsylvania, USA.

[2]Departments of Genetics and Pediatrics; Epigenetics Institute; Institute of Regenerative Medicine; Center for Research on Reproduction and Women's Health; University of Pennsylvania Perelman School of Medicine, Philadelphia, Pennsylvania, USA.

[3]Division of Neonatology; Children's Hospital of Philadelphia, Philadelphia, Pennsylvania, USA.

[4]Departments of Physiology and Neuroscience; University of Pennsylvania Perelman School of Medicine, Philadelphia, Pennsylvania, USA.

[5]Department of Biochemistry and Molecular Biophysics; Washington University School of Medicine, St. Louis, Missouri, United States

[†]To whom correspondence should be addressed: roberto@bonasiolab.org; metalsga@gmail.com

ABSTRACT

RNAs move through the extracellular space to transmit information between cells, including mammalian neurons, yet how specific RNAs are channeled into these extracellular routes is unknown. Using genome-wide CRISPR screening, proteomics, and high-sensitivity transcriptomics in a neuronal cell line, we identify domesticated retroviral proteins and RNA-modifying enzymes that regulate RNA loading into and transportation via extracellular vesicles. We show that the pseudouridine synthase PUS1 is a key determinant of RNA trafficking, and that its catalytic product in RNA, pseudouridine, is both necessary and sufficient for extracellular RNA export. We further show that myosin light chain 6 (MYL6) is a pseudouridine-binding protein required for secretion of synthetic and endogenous RNAs. These findings reveal a biochemical code linking chemical RNA modification to extracellular transport, and establish a framework to study the function of extracellular RNAs in the nervous system and beyond.

INTRODUCTION

Cells exchange information to coordinate their actions. In addition to hormones, neurotransmitters, and other small molecules, RNAs also cross the plasma membrane and traverse the extracellular space to exert regulatory functions across cellular, tissue, and sometimes organismal boundaries (Betti et al., 2021; Cai et al., 2018; Kaletsky et al., 2020; Maori et al., 2019; Molnar et al., 2010; Tassetto, Kunitomi, & Andino, 2017). In mammals, such intercellular transfer of RNA has been associated with diverse physiological and pathological processes, including brain function and disease (Budnik, Ruiz-Canada, & Wendler, 2016; Huo, Du, Li, Liu, & Xu, 2021; Marangon, Castro, & Lecca, 2022; Z. Y. Wang, Wen, Xu, Zhang, & Zhang, 2022), cancer (Moller & Lobb, 2020) and intergenerational epigenetic inheritance (Conine & Rando, 2022), but its mechanistic basis remain obscure. Here, we investigate how RNAs are selected for extracellular export, a necessary step toward understanding what type(s) of information they communicate between cells, and determining whether and how this process affect phenotypic, transcriptional, and epigenetic states.

Extracellular RNAs (exRNAs) are often found within extracellular vesicles (EVs), membrane-based particles of heterogenous size, origin, and composition (van Niel, D'Angelo, & Raposo, 2018; Welsh et al., 2024), produced by most cell types (Deatherage & Cookson, 2012), and capable of transferring their cargo between cells (O'Brien, Breyne, Ughetto, Laurent, & Breakefield, 2020). Other structures, including membrane-free ribonucleoprotein complexes (Murillo et al., 2019; Tosar & Cayota, 2020) and virus-like particles (Ashley et al., 2018; M'Angale et al., 2025; Moore et al., 2021; Pastuzyn et al., 2018; Segel et al., 2021), can also transport RNA through the extracellular environment, although these processes are even less well understood than those mediated by canonical EVs.

The exRNAs produced by a given cell type do not recapitulate its intracellular RNA content (Cha et al., 2015; Mittelbrunn et al., 2011; Shurtleff et al., 2017; Upton et al., 2021; Valadi et al., 2007), suggesting the existence of molecular pathways that facilitate (select) or prevent (filter) the release of specific RNAs in the extracellular environment. Mechanisms for exRNA selection have been proposed, including sequence-specific sorting mediated by RNA-binding proteins (Garcia-Martin et al., 2022; Leidal et al., 2020; Santangelo et al., 2016; Shurtleff, Temoche-Diaz, Karfilis, Ri, & Schekman, 2016; Shurtleff et al., 2017; Villarroya-Beltri et al., 2013) and selective processing of exRNAs after their release (Costa et al., 2023; Nechooshtan, Yunusov, Chang, & Gingeras, 2020; Tosar et al., 2020). To date, mechanistic studies have focused on extracellular transport mechanisms for miRNAs, which are more easily captured with traditional small RNA

47 sequencing protocols (Gustafsson et al., 2025; Scacchetti et al., 2024), and largely utilized non-
48 neuronal cell lines. However, miRNAs are relatively scarce in EVs (Chevillet et al., 2014), and it
49 is becoming increasingly clear that neurons might have specialized strategies to select and
50 release exRNAs (Ashley et al., 2018; Bervoets et al., 2024; M'Angale et al., 2025; Pastuzyn et al.,
51 2018). Hence, the full spectrum of mechanisms that participate in exRNAs selection and transport,
52 especially in neurons, remain unknown.

53 Here, we describe a novel genetic screen that uncovered new regulators of exRNA export in a
54 neuronal cell line. These include domesticated retroviral proteins and RNA-modifying enzymes.
55 Among the latter, we show that the pseudouridine synthetase 1 (PUS1) and its catalytic product,
56 pseudouridine (Ψ), are necessary and sufficient for the selection and extracellular release of
57 certain exRNAs, including full-length tRNAs and snoRNAs.

58 RESULTS

59 Neuronal CADs produce RNA-containing EVs

60 To investigate the genetic and biochemical determinants of neuronal exRNA biogenesis in a
61 tractable model, we selected Cath.a-differentiated cells (CADs), an immortalized cell line that
62 resembles catecholaminergic neurons and is capable of forming neurite-like structures under
63 serum-free conditions (Mews et al., 2017; Qi, Wang, McMillian, & Chikaraishi, 1997; H. Wang &
64 Oxford, 2000). We isolated EVs from conditioned, serum-free medium from CAD cultures using
65 an established serial ultracentrifugation method (**Fig. 1A**) (Thery, Amigorena, Raposo, & Clayton,
66 2006). This relatively crude EV fraction consisted primarily of particles ranging from 90 to 150 nm
67 in diameter (median 123 nm, **Fig. 1B**), consistent with the expected size range of small EVs
68 (Welsh et al., 2024). This fraction was enriched for known EV markers (SDCBP, PDCD6IP/ALIX,
69 TSG101, CD9), and depleted for conventional control mitochondrial and ER proteins (COXB5 and
70 CANX) (**Fig. 1C**) (Kugeratski et al., 2021). Overall, 81% of the proteins enriched in our EV isolate
71 also appeared in a curated database of EV components (Vesiclepedia, **Fig. S1A**) (Chitti et al.,
72 2024), and gene ontology (GO) annotations for the proteins we identified in CAD EVs were
73 enriched for relevant terms, including "*intracellular vesicle*" and "*endosome*" (**Fig. 1D**). Consistent
74 with the neuronal identity of CADs, GO terms associated with neurons ("*synaptic membrane*",
75 "*axon*") were also enriched, as well as specific neuronal EV markers L1CAM and ATP1A3 (You
76 et al., 2023) (**Fig. 1C**, **Table S1**).

77 In contrast to the intercellular RNA composition of CADs, their EVs contained predominantly small
78 RNA species (< 500 nts; **Fig. 1E**), as previously observed in other neuronal EVs (Bellingham,
79 Coleman, & Hill, 2012). Because conventional, ligation-based protocols to sequence small RNAs
80 were predominantly developed to detect miRNAs (Crocker, Trigg, & Conine, 2022; Gustafsson
81 et al., 2025), we used LIDAR sequencing (Scacchetti et al., 2024), which captures a broader
82 range of RNAs regardless of their size and chemical modifications, to obtain a comprehensive
83 profile of the exRNAs produced by CADs. LIDAR revealed 2,854 RNAs that were significantly
84 (adjusted p value < 0.1) enriched in EVs compared to whole-cell extract (**Fig. 1F**). Compared to
85 the intracellular transcriptome, CAD exRNAs were enriched for nuclear tRNAs, Y-RNAs, and
86 some snRNAs, and depleted for mitochondrial tRNAs and miRNAs (**Fig. 1G; S1B**). Some classes
87 of snoRNAs such as the H/ACA box family were enriched in EVs, whereas others, such as C/D
88 box snoRNAs were more abundant inside the cells (**Fig. S1C**). Careful inspection of the reads
89 mapping to tRNA genes revealed the presence in EVs of a mixture of full-length tRNAs and
90 various types of tRNA-derived fragments (tDRs) (**Fig. S1D–E**).

91 Thus, CADs produce EVs that contain known EV-associated proteins, as well as neuron-specific
92 proteins, and these EVs carry a variety of exRNAs, including full-length tRNAs and their
93 fragments.

94 **Transduced sgRNAs are loaded into EVs**

95 The fact that CAD EVs are enriched for specific RNAs when compared to their intracellular content
96 suggests the presence of dedicated pathways ensuring that only certain transcripts are selected
97 to become exRNAs. Potential mechanisms for both active and passive regulation of RNA
98 secretion have been proposed (Tosar, Witwer, & Cayota, 2021), but very few examples,
99 seemingly dedicated to the export of specific miRNAs, have been demonstrated (Garcia-Martin
100 et al., 2022; Liu, Ma, & Schekman, 2021; Shurtleff et al., 2017; Villarroya-Beltri et al., 2013). It is
101 unclear whether these bespoke pathways also affect other RNA classes, which constitute the
102 majority of exRNAs (**Fig. S1B**).

103 In search for general regulators of exRNA biogenesis, we perform a genome-wide knockout
104 screen. In a typical CRISPR/Cas9 screen, a library of single-guide RNAs (sgRNAs) targeting
105 genes of interest (or all genes in the case of genome-wide screens) is transduced into cells that
106 are then selected for a phenotype, for example drug resistance. Enriched or depleted sgRNAs
107 provide information on genes that regulate that phenotype and are identified by sequencing the
108 encoding transgenes integrated into the genome of the selected cells, thus linking genotypes to

109 phenotypes. This approach cannot be used for phenotypes not physically connected to the cell of
110 origin, such as EV abundance and composition.

111 We made the serendipitous observation that transduced sgRNAs could be detected, albeit at a
112 low level, in the crude EV fraction from CADs (**Fig. S2A**), therefore coupling the sgRNA genotype
113 of the originating cell to phenotypes associated with the sgRNA-containing EVs (**Fig. 2A, S2B**).
114 We reasoned that knockout of genes required for EV production or for loading RNAs into EVs
115 would result in the disappearance of the corresponding sgRNAs from the EV fraction, allowing us
116 to perform a genome-wide screen to identify genes involved in these processes.

117 We envisioned that all targeted genes and the corresponding sgRNAs would fall within 4 possible
118 categories (**Fig. 2B**)**:** 1) sgRNAs not affecting viability, EV production, or RNA export ("no effect")
119 would remain constant over time in both cells and EVs; 2) sgRNAs targeting genes promoting
120 survival or proliferation would be depleted over time in both intracellular and extracellular pools
121 ("essential"); 3) positive regulators of EV production or RNA export would become less abundant
122 in the EV-associated pool over time, while possibly accumulating within cells ("positive"); and 4)
123 *vice versa* for negative regulators ("negative").

124 **A genome-wide screen for EV regulators**

125 We transduced CADs with the genome-wide Brie library, comprising ~80,000 sgRNAs targeting
126 ~20,000 protein-coding genes (**Fig. 2A**) (Sanson et al., 2018). Two days after infection, we
127 harvested a fraction of the cells and EVs to quantify baseline sgRNA distribution. Eight days later
128 (day 10 after transduction), we harvested cells and EVs again, and prepared libraries to sequence
129 the sgRNAs, using a modified LIDAR protocol (**Fig. S2C**). We performed the screen twice,
130 obtaining two independent experimental replicates.

131 Deep sequencing detected > 95% of sgRNAs in all samples (**Fig. S2D**). As early as day 2 after
132 transduction, likely before most knockout effects would manifest, not all sgRNAs were equally
133 represented in EVs vs. cells (**Fig. S2E**), indicating that some sgRNAs are more likely to be loaded
134 into EVs than others. This suggests that these exogenous RNAs are likely subjected to the same
135 selection processes that act on endogenous RNAs, potentially influenced by differences in
136 sequence, structure, or both. Consistent with this, sgRNAs that were preferentially exported as
137 exRNAs were characterized by a higher frequency of uridines at the 5' (**Fig. S2F**), raising the
138 possibility that these uridines, or perhaps their chemical modification, might contribute to the
139 selection process.

140 We analyzed the relative changes in abundance of sgRNAs in cells and EVs over time and sorted
141 the sgRNAs in the four categories described above (**Fig. 2C**). As expected, most sgRNAs were
142 neither enriched nor depleted ("no effect"), while sgRNAs targeting reported essential genes, such
143 as *Pcna*, *Cdk1*, and *Rrm1* were depleted at day 10 compared to day 2, both in cells and in EVs
144 ("essential"). Single-guide RNAs targeting tetraspanins, *Cd63*, *Tspan6*, and *Tspan15* were
145 depleted at day 10 in EVs, but not inside the cells, where they were either unchanged or enriched.
146 This indicates that these genes might function as positive regulators of EV biogenesis ("positive"),
147 in line with their known role in membrane trafficking (Toribio & Yanez-Mo, 2022). Conversely, we
148 observed an enrichment of sgRNAs in EVs, but not in cells, ("negative") for two subunits of ESCRT
149 complexes, *Tsg101* and *Hgs* (*Hrs*), consistent with recent reports suggesting that they may
150 function as negative regulators for release of some EV subtypes (Kunitake et al., 2024; Matsui,
151 Osaki, Hiragi, Sakamaki, & Fukuda, 2021). *Vps51*, encoding a subunit of the GARP complex
152 (Conibear, Cleck, & Stevens, 2003), was also classified by our screen as a negative regulator,
153 likely due to its role in mediating retrograde trafficking from early endosomes to the Golgi
154 apparatus (Reggiori, Wang, Stromhaug, Shintani, & Klionsky, 2003).

155 For each sgRNA, we calculated a "predicted" abundance in EVs compared to cells at day 10
156 based on the export efficiency measured at day 2 and then determined deviations from this
157 predicted value in the "observed" sgRNA abundances. Overall, we identified 1,275 and 1,228
158 genes targeted by significantly (p value < 0.05) depleted or enriched sgRNAs (**Fig. 2D; Table**
159 **S2**), and therefore likely to function as positive or negative regulators of exRNA
160 selection/transport, respectively. Overall, the candidate positive regulators in our screen were
161 enriched for GO terms related to known EV biogenesis routes, such as "*late endosome*",
162 "*multivesicular body*", and "*extracellular vesicle*" (**Fig. 2E**), and comprised various genes involved
163 in the regulation of EV production and release (*Tspan6*, *Cd63*, *Flot1*, *Smpd3*, *Vps37c*, *Chmp2a*,
164 *Chmp5*, and *Chmp7*) (**Fig. 2D**). Among these, *Sdcbp* (**Fig. 2D; S2G**) stood out because of its
165 demonstrated role in EV biogenesis (Baietti et al., 2012), established use as marker for these
166 structures (Kugeratski et al., 2021), and abundance in CAD EVs (**Fig. 1C**). To confirm its function
167 in neuronal EVs, we generated two independent *Sdcbp*$^{-/-}$ CAD cell clones (**Fig. S2H**). Loss of
168 SDCBP caused reduced particle numbers indicative of impaired EV production, consistent with
169 the effects observed in other cell types (Baietti et al., 2012) (**Fig. S2I–J**).

170 As our screen utilized extracellular sgRNAs directly as a readout, the identification of *Sdcbp*
171 suggests that sgRNAs are exported, at least in part, via EVs originating from a variation of the
172 ESCRT pathway (Baietti et al., 2012). However, several genes coding for domesticated retroviral

173 proteins (*Arc, Moap1, Nynrin, Pnma8b, Rtl5, Rtl8b*) (Henriques et al., 2024) were also among the
174 top candidates for positive regulators of sgRNA export (**Fig. 2F**). Encapsulation of RNAs in
175 capsid-like structures could therefore represent an alternative route for exRNA export, potentially
176 one reserved for neuronal cells (Al Othman et al., 2024; Ashley et al., 2018; Madigan et al., 2024;
177 Pastuzyn et al., 2018; Xu et al., 2024), given that several of these genes are preferentially
178 expressed in the nervous system (Henriques et al., 2024). Consistent with neuronal-biased
179 expression, all of these candidates except *Moap1* (for which our RNA-seq was not sufficiently
180 sensitive) were upregulated upon differentiation of CADs into their mature neuronal phenotype
181 (**Fig. S2K**) (Mews et al., 2017; Qi et al., 1997).

182 Our screen also identified several positive regulators with no obvious link to membrane trafficking.
183 We reasoned that some of these factors might be involved in RNA selection or loading into the
184 EVs and that, therefore, their depletion would cause the disappearance of the corresponding
185 sgRNAs over time. Amongst them, we noted several enzymes responsible for installing or
186 removing chemical modifications on RNA, including pseudouridine (*Pus1, Rpusd2*) (Rintala-
187 Dempsey & Kothe, 2017), wybutosine (*Tyw1*) (Sun et al., 2024), acp(3)uridine (acp^{3}U) (*Dtwd1*)
188 (Takakura, Ishiguro, Akichika, Miyauchi, & Suzuki, 2019), mannosyl-queuosine (*Gtdc1*) (Zhao et
189 al., 2023), inosine (*Adarb1*) (J. B. Li & Walkley, 2025) , methyl groups (*Mrm2*) (Rorbach et al.,
190 2014), and amino acids (*Vars1, Tars1, Tars2, Dtd2, Prorsd1*) (Kuncha et al., 2018; Ruan, Zhou,
191 Tan, & Wang, 2013; Rubio Gomez & Ibba, 2020) (**Fig. 2G**). More broadly, we identified 224 RNA-
192 binding proteins amongst the positive exRNA regulators via RBP2GO analysis (Caudron-Herger,
193 Jansen, Wassmer, & Diederichs, 2021) (**Table S3**), in line with our expectations that factors
194 involved in the selection and loading of RNAs into EVs would be revealed by our genetic screen.

195 In summary, we devised a pooled genome-wide strategy to link genetic perturbation to regulation
196 of exRNA export. We identified several factors that could be promoting or restricting exRNA
197 selection and transport, including several domesticated retroviral genes, suggesting an
198 alternative, potentially neuron-specific mode of RNA secretion. Our screen also uncovered a
199 variety of RNA modifiers and RNA-binding proteins that could be involved in marking and
200 selecting specific RNAs for extracellular trafficking, as demonstrated below for PUS1.

201 **PUS1 shapes the neuronal exRNA population**

202 Among the RNA-modifying enzymes identified as candidate positive regulators of exRNAs, we
203 chose to focus on the pseudouridine (Ψ) synthase PUS1 (Rintala-Dempsey & Kothe, 2017),
204 because it was among the top 100 most significant positive regulators (**Fig. 2D, G; Table S2**) and

205 because genetic evidence supports a role for Ψ in RNA mobility in *Arabidopsis thaliana* pollen
206 (Herridge et al., 2025).

207 To validate the results of the screen, we utilized an orthogonal, pooled CRISPR interference
208 approach (CRISPRi) (Kampmann, 2018), whereby we knocked down genes of interest by
209 repressing their transcription with dCas9-KRAB guided by sgRNAs different from to those used
210 for the primary screen (**Fig. S3A**). CRISPRi of *Pus1* in CADs suppressed the secretion of sgRNAs
211 significantly ($p = 0.01$) and to a larger extent than the positive control *Sdcbp* (**Fig. S3B**), confirming
212 its involvement in exRNA export.

213 To determine the contribution of PUS1 to the export of endogenous RNAs, we profiled intra- and
214 extra-cellular RNAs in wild type CADs and two independent *Pus1*$^{-/-}$ clones (**Fig. 3A**). Loss of
215 PUS1 resulted in a significantly (adjusted p value < 0.1) altered profile of 560 exRNAs, skewed
216 more than 2-fold toward reduced export (390 reduced vs. 170 increased exRNAs; **Fig. 3B**).
217 Changes in exRNA abundance were not secondary to altered levels of the corresponding
218 transcripts inside the cells, as shown by a negligible overlap in the affected RNA subsets (**Fig.
219 3C; S3C–E**). The export of miRNAs, snoRNAs, and both mitochondrial and nuclear tRNAs was
220 significantly impaired in the absence of PUS1 compared to wild type (**Fig. 3D**). Further inspection
221 of tRNA-mapping reads revealed that full-length and 5' and 3' tRNA-derived fragments (tDRs;
222 **Fig. 3E**) were exported less efficiently into EVs in absence of PUS1, with the full-length transcripts
223 being most strongly affected (**Fig. 3F**).

224 We conclude that PUS1 is necessary for the secretion of certain RNAs, including miRNAs,
225 snoRNAs, and tRNAs, in CADs.

226 **Pseudouridine installed by PUS1 is enriched in exRNAs**

227 Based on our observation that PUS1 is required for the release of a subset of exRNAs, we
228 hypothesized that its catalytic product, Ψ, might guide certain RNAs to be incorporated into EVs,
229 facilitating their export into the extracellular space.

230 To determine if exRNAs contain Ψ , we incorporated the Ψ-bisulfite adduct production step from
231 BID-seq (Dai et al., 2023) into our high-sensitivity LIDAR approach (Scacchetti et al., 2024). This
232 allowed us to identify Ψ through the appearance of microdeletions in the sequencing reads (**Fig.
233 4A**), as demonstrated on a synthetic RNA (**Fig. S4A**) and within endogenous 18S rRNA, which
234 contains several known Ψ residues (**Fig. S4B**) (Dai et al., 2023). With this approach, we detected
235 1,111 Ψ sites on 466 distinct exRNAs from CADs (**Fig. S4C–D**). As expected, most Ψ sites were

236 within tRNAs both inside and outside the cells, but RNAs from other classes also contained this
237 modification, (**Fig. 4B**), consistent with existing observations (Schwartz et al., 2014).

238 The majority of exRNAs with detectable Ψ also carried this modification inside the cells (**Fig.**
239 **S4C**), in most cases at the same exact sites (**Fig. S4D**)**;** however, we observed higher Ψ levels
240 on exRNAs compared to cellular RNAs (**Fig. 4C**), suggesting an association of the mark with their
241 extracellular export.

242 Next, we sought to determine whether Ψ was also enriched on physiologically relevant exRNAs
243 *in vivo*. We isolated RNA from EVs purified from the cauda section of the mouse epididymis, (**Fig.**
244 **4D; S4E**), where RNAs are transferred to the developing sperm via specialized EVs
245 (epididymosomes) in a process necessary for proper sperm function (Trigg & Conine, 2024) and
246 implicated in intergenerational inheritance (Conine & Rando, 2022). Using bisulfite-modified
247 LIDAR, we identified 1,976 Ψ sites on 846 cauda exRNAs. As observed in CADs, cauda exRNAs
248 contained higher levels of Ψ compared to their intracellular counterparts (**Fig. 4E**), demonstrating
249 that Ψ is enriched on exRNAs not only *in vitro* (see **Fig 4C**), but also *in vivo*.

250 Our genetic evidence (**Fig. 2–3**) and sequencing results (**Fig. 4C, E**) support the hypothesis that
251 conversion of U to Ψ by PUS1 on facilitates the secretion of select RNAs. To test this hypothesis,
252 we sought to determine whether the loss of PUS1-dependent Ψ in CADs would cause decreased
253 export of specific exRNAs. Because Ψ can also be deposited by other enzymes, we first identified
254 uridines specifically modified by PUS1, by comparing bisulfite-induced deletions in exRNAs from
255 *Pus1*$^{-/-}$ vs. wild type CADs and found 479 PUS1-dependent Ψ sites on 270 transcripts, accounting
256 for 43% of the total Ψ sites on exRNAs (**Fig. 4F**). Decreased Ψ levels on these PUS1 targets did
257 not affect their abundance inside the cells compared to RNAs containing Ψ residues unaffected
258 by PUS1 loss (**Fig. 4G**, left). However, the abundance of PUS1 targets in the EVs from *Pus1*$^{-/-}$
259 CADs was significantly decreased (**Fig. 4G**, right) (p = 0.008) suggesting that Ψ was required for
260 their efficient export.

261 The majority of exRNAs carrying PUS1-dependent Ψ were full-length tRNAs (**Fig. S4F–G**), which
262 were targeted by PUS1 specifically at position 27 and 28 of the anticodon stem (**Fig. S4H–J**), as
263 previously reported in other cell types (Schwartz et al., 2014). Of the 8 full-length tRNAs that were
264 significantly depleted in EVs from *Pus1*$^{-/-}$ CADs, all but 1 (Fisher's test p = 0.006) contained a
265 PUS1-dependent Ψ at position 27 or 28 (**Fig. S4K**), as exemplified for *tRNA-Arg-CCG-3-1*, *tRNA-*
266 *Arg-CCT-4-1, tRNA-Ile-AAT-1-1,* and *tRNA-Val-CAC-2-1* (**Fig. 4H–I**)

267 Not all Ψ sites on these extracellular tRNAs were PUS1 sensitive, as shown by the persistence
268 of Ψ signal at other positions in *Pus1*$^{-/-}$ KOs (**Fig. S4I**), most notably base 54, which is known to
269 be modified by PUS10 (**Fig. S4J**) (Schwartz et al., 2014). This indicates that the role of Ψ in the
270 export of these exRNAs is context-dependent, and that sequence or structural features of the
271 surrounding RNA (or possibly additional RNA modifications) contribute to its function.

272 We observed a similar exRNA export defect in *Pus1*$^{-/-}$-derived EVs for snoRNAs (**Fig. S4L**),
273 although in this case only 6 out of 13 snoRNAs containing PUS1-sensitive sites displayed an
274 export defect in the knockout cells, as exemplified by *Snord59a* and *Snord87* (**Fig. 4J–K)**.

275 Together, these observations support the conclusion that selective Ψ deposition by PUS1 on
276 specific RNAs is necessary to guarantee their efficient extracellular export.

277 **Ψ stimulates RNA secretion through MYL6**

278 Given that Ψ is enriched on exRNAs and that PUS1 facilitates their export into the extracellular
279 space (see **Fig. 3–4**), we wondered if Ψ is sufficient to induce RNA secretion. We *in vitro*
280 transcribed 102 bp-long RNAs replacing all U's with Ψ. We transfected these Ψ-containing RNA
281 into CADs and measured their appearance in the extracellular space by RT-qPCR after 24 hours
282 (**Fig. 5A**). RNA containing Ψ was exported ~4 times more efficiently compared to the U-containing
283 control, despite their levels being the same inside the cells (**Fig. 5B**). We tested additional RNAs,
284 differing in sequence at their 5' (**Table S5**) and for most of them (4 out of 6 sequences tested) the
285 presence of Ψ resulted in significantly increased abundance outside the cells, with a fifth one
286 (RNA #6) also showing a clear trend toward increased export (**Fig 5C**). Overall, these results
287 indicate that the presence of Ψ on an RNA is sufficient, in most cases, to stimulate its extracellular
288 export.

289 We hypothesized that one or more RNA-binding protein might recognize Ψ-marked RNAs to
290 channel them into secretory pathways. We incubated biotinylated RNA containing Ψ or only U's
291 as control with CAD whole-cell extracts, purified the RNA with streptavidin, and analyzed
292 associated proteins via mass spectrometry. 46 proteins bound specifically to Ψ-containing RNA
293 compared to the U-only control (**Fig. S5A; Table S4**), among which the myosin light chain 6
294 (MYL6) was the most enriched Ψ-specific binder (**Fig. 5D; Table S4**). MYL6 is an essential light
295 chain component of the non-muscle myosin II complex (Brito & Sousa, 2020), and it was
296 previously reported as a putative non-canonical RNA-binding protein (Caudron-Herger et al.,
297 2019).

298 Consistent with a potential role in exRNA trafficking, MYL6 was enriched in the proteome from
299 CAD EVs (**Fig. 1C; Fig. S5B**) and sgRNAs against it were depleted in our screen, although slightly
300 below our significance threshold (p = 0.053) (**Fig. S5C**). We knocked down MYL6 in CADs (**Fig.**
301 **S5D**) and found that the Ψ-dependent secretion of 2 out of 4 RNAs was substantially impaired,
302 with a third one also demonstrating a clear trend toward reduction (**Fig. 5E**). To determine whether
303 MYL6 was also involved in the Ψ-dependent export of endogenous exRNAs we performed LIDAR
304 on intra- and extra-cellular RNAs after MYL6 knockdown. The abundance of intracellular RNAs
305 was largely unaffected (**Fig. S5E**); however, the export of specifically Ψ-containing exRNAs was
306 significantly impaired by MYL6 knockdown (**Fig. 5F–G).**

307 Our results demonstrate that the presence of Ψ—a modification enriched on exRNAs *in vitro* and
308 *in vivo*—is sufficient to stimulate exRNA export, and that, in many cases, Ψ-mediated exRNA
309 sorting is an active process mediated by the non-canonical RNA-binding protein MYL6.

310 DISCUSSION

311 In this study, we combined biochemical, genetic, and genomic approaches to reveal a role for
312 PUS1 and MYL6 in guiding the extracellular traffic of RNAs via Ψ. We propose a model
313 whereby PUS1 labels select RNAs with Ψ at defined sites, which are then bound by MYL6 to be
314 packaged into EVs and secreted (**Fig. 5H**). In addition to PUS1 and MYL6, our work points to
315 many new candidate regulators that might play important roles in selecting (RNA-modifying
316 enzymes) and transporting (domesticated retroviral proteins) RNAs from neurons and other cell
317 types into the extracellular space.

318 A genome-wide screen for EV and exRNA regulators

319 We developed a CRISPR/Cas9 pooled genetic screen strategy that linked extracellular
320 phenotypes to cellular genotypes via direct sequencing of secreted sgRNAs (**Fig. 2; S2**). With
321 this design, we could identify not only factors that regulate EV biogenesis in general, but also
322 factors required for the selection, loading, and transport of exRNAs into EVs, and potentially other
323 non-canonical RNA-containing extracellular particles.

324 Two other screens aimed at separately addressing one or the other process have been published
325 to date. In one case, artificial tethering of sgRNAs though an EV-specific anchor (CD63-dCas9 or
326 CD9-dCas9) was used to create a readout for EV production (Kunitake et al., 2024), which limited
327 the screen to the discovery of factors regulating the biogenesis of these specific EV sub-
328 populations containing CD63 or CD9, and, by design, bypassed the factors required to load RNA

329 into the EVs. In the other, barcoded miRNAs containing the EXO motif (Villarroya-Beltri et al.,
330 2013) were used as reporters for miRNA secretion, revealing the role of ARHGEF18 in regulating
331 the release of miRNA-containing EVs (Lu et al., 2018). In this latter case, only factors involved in
332 movement of this specific subset of exRNAs could be recovered.

333 While these two studies provided important insights into EVs and miRNA transport, respectively,
334 our unbiased screen cast a broader net for general regulator of all extracellular particles
335 containing exRNAs, as revealed by the extensive number of "hits" already known to take part in
336 membrane trafficking (**Fig. 2D–E**), and by the large number of candidates involved in RNA
337 biology, such as RNA-modifying enzymes (**Fig. 2G**), that have not been previously linked to RNA
338 secretion.

339 Importantly, ours was the first genetic screen for an EV phenotype to be conducted on a neuronal
340 cell line, which, in addition to its unique and broader design, likely contributed to our ability to
341 detect several candidates not previously associated with exRNA trafficking and that might be
342 restricted—in expression or function—to the nervous system.

343 **Routes of exRNA secretion in neurons**

344 While we designed our genetic screen with the goal of uncovering specific regulators of exRNA
345 selection and export, the strategy allowed us to simultaneously identify several factors involved
346 in the biogenesis and trafficking of EVs as "by-products". The observation that SDCBP was
347 identified as positive regulator (**Fig. S2G–J**) suggests that sgRNAs (and other RNAs) taking the
348 extracellular route may be loaded into EVs formed through a variation of the canonical ESCRT
349 pathway, in which SDCBP acts in concert with ALIX to regulate the production of endosomal
350 intraluminal vesicles (Baietti et al., 2012). This is further supported by the presence of several
351 components of the ESCRTIII complex (CHMP2A, CHMP5, CHMP7) amongst the list of candidate
352 positive regulators (**Fig. 2D**). We also recovered factors involved in alternative modes of exRNA
353 secretion in neuronal cells, such as intraluminal vesicles produced by endosomal membrane
354 curvatures induced by ceramide in lipid rafts (Dixson, Dawson, Di Vizio, & Weaver, 2023), since
355 both SMPD3 (nSmase2, responsible for ceramide synthesis) and FLOT1 (enriched in lipid rafts)
356 appeared amongst our positive regulators of exRNAs (**Table S2**).

357 In line with the neuronal identity of CADs, but somewhat unexpectedly, we detected synaptic
358 components in our EV preparation (**Fig. 1D; Table S1**) and some of them (e.g.: CXADR, GNAO1,
359 CNR1, ADAM10) were also identified as exRNA regulators in our screen (**Fig. 2E; Table S2**).
360 This suggests that in mammalian neurons, some EVs are produced at the presynaptic membrane,

361 as observed in *Drosophila* (Blanchette et al., 2022; Korkut et al., 2009), indicating the existence
362 of a dedicated, alternative route for neuronal exRNAs. Interestingly, fly and mammalian neurons
363 have been shown to package RNAs for secretion in structures resembling viral capsids originating
364 from domesticated retroviral proteins (Erlendsson et al., 2020; M'Angale et al., 2025; Pastuzyn et
365 al., 2018), whose intercellular exchanges appears important for synaptic function, as well as
366 learning and memory formation (Sullivan, Ravens, Walker, & Shepherd, 2025).

367 Among potentially neuron-specific regulators of exRNA trafficking, domesticated retroviral
368 proteins stand out as particularly intriguing, with six recovered in our screen (**Fig. 2F**). One of
369 these, ARC, is a GAG homolog that assembles into a virus-like particle that transports its own
370 mRNA across the plasma membrane in humans and flies (Al Othman et al., 2024; Ashley et al.,
371 2018; Pastuzyn et al., 2018). Several additional genes with homology to the retroviral GAG capsid
372 protein or other retroviral components are under purifying selection in mammalian genomes
373 (Henriques et al., 2024) and their expression is often high in the nervous system, hinting at the
374 tantalizing possibilities that brains have hijacked viral machinery for the purpose of RNA-based
375 communication.

376 **Biochemical rules of exRNA selection**

377 The most obvious class of candidate positive regulators of exRNAs revealed by our screen were
378 RNA-modifying enzymes (**Fig. 2G**). Among these, we chose to focus on PUS1 (see below);
379 however, not all pseudouridylated exRNAs depend on PUS1 for their secretion, and many
380 exRNAs do not contain Ψ. We suspect that other RNA modifying enzymes contribute—
381 independently or in concert with PUS1—to shape the exRNA population in neurons and other cell
382 types.

383 Among these other candidates, we note DTWD1, an enzyme responsible for acp^3U deposition on
384 tRNAs and possibly other substrates (Takakura et al., 2019). acp^3U is an attachment site for N-
385 glycans (Xie et al., 2024), and glycosylation of some RNAs seems to be important for their
386 secretion through EVs (Sharma, Jiao, Yang, Kwan, & Kiledjian, 2025), suggesting that glycans
387 could serve as alternative exRNA selection marks. Furthermore, we identified ALKBH6 (**Table**
388 **S2**), a poorly characterized protein predicted to have RNA demethylase activity (Ma et al., 2022),
389 as one of the top negative regulators (i.e.: factors that restrict exRNA export). A related RNA
390 demethylates ALKBH5 was recently shown to prevent RNA secretion via m6A removal (Chen et
391 al., 2025), and we speculate ALKBH6 may function similarly as a “filter” for exRNA export via
392 modulation of RNA methylation on yet unknown RNA substrates.

393 Our screen also uncovered hundreds of RNA-binding proteins that may regulate RNA secretion
394 without modifying them enzymatically (**Table S3**). Among these, we identified VAP-A, an
395 important regulator of exRNA export, previously reported to load RNAs into intraluminal vesicles
396 at contact sites between endoplasmic reticulum and multivesicular bodies (Barman et al., 2022).
397 We also identified ANXA7, a protein involved in regulating membrane fusion during exocytosis
398 (Caohuy & Pollard, 2002) and recently reported as an RNA binder (Tartaglia, Hollas, Havik,
399 Vedeler, & Pastore, 2025). Given its enrichment in CAD EVs (**Table S1**) and its reported
400 interaction with ESCRT-III (Sonder et al., 2019), we postulate it may additional function as an
401 RNA cargo loader during EV formation. On the other hand, we failed to identify some other RNA-
402 binding proteins previously shown to modulate exRNA export, such as ALYREF, FUS, ATG7/12,
403 SYNCRIP, YBX1, and HNRNPA2B1(Garcia-Martin et al., 2022; Leidal et al., 2020; Santangelo et
404 al., 2016; Shurtleff et al., 2016; Shurtleff et al., 2017; Villarroya-Beltri et al., 2013). This could be
405 due to ineffectiveness of sgRNAs, reporter RNA, or cell type used. In fact, we deem it likely that
406 different cell types utilize different sets of RNA-binding proteins and RNA modifications to guide
407 the secretion of different classes of RNAs.

408 **A role for Ψ on exRNAs**

409 Ψ is the most abundant RNA modification found in cells, and it is known for its roles in RNA
410 stability, translation, and splicing (Cerneckis, Cui, He, Yi, & Shi, 2022). However, the very strong
411 depletion of sgRNAs against PUS1 in our screen, as well as some indirect evidence in other
412 organisms motivated us to explore a potential role in exRNAs. In *Arabidopsis*, Ψ appears to
413 participate to the transfer of small RNAs from pollen to sperm cells (Herridge et al., 2025). In
414 human colorectal cancer cells, decreased Ψ levels caused by 5-fluorouracil treatment were linked
415 to alteration of extracellular small RNA profiles (Qu et al., 2024). In line with these reports, we
416 found Ψ to be 1) enriched in exRNAs both from CAD cell cultures and mouse tissue, 2) sufficient
417 for export of most synthetic RNAs tested, and 3) required for the release of endogenous RNA,
418 especially tRNAs and snoRNAs, into the extracellular space.

419 How does Ψ promote RNA secretion? We propose that the conversion of U to Ψ creates new
420 binding sites for specific proteins—Ψ readers. We identified MYL6, part of the non-muscle myosin
421 II complex, as a putative new Ψ reader and demonstrated its functional involvement in RNA export
422 of synthetic and endogenous exRNAs marked by Ψ **(Fig. 5**). Intriguingly, other cytoskeletal
423 proteins, such as the actin-binding protein PFN1, have been reported to interact with Ψ (Wei et
424 al., 2025). RNAs containing Ψ might thus “hitchhike” cytoskeletal components to be loaded into
425 vesicles and eventually secreted, a pathway already proposed for other vesicular cargo such as

426 actin-associated proteins (Holliday, Faria, & Rody, 2019). It is worth noting, however, that not all
427 Ψ-containing synthetic and endogenous exRNAs were sensitive to MYL6 depletion **(Fig. 5G**).
428 While this could be attributed to experimental limitations (such as incomplete knockdown), it is
429 also possible that other Ψ readers are involved, perhaps in an RNA sequence- or structure-
430 dependent fashion.

431 PUS1 is a conserved eukaryotic standalone pseudouridine synthetase which has been
432 extensively characterized in *S. cerevisiae* (Rintala-Dempsey & Kothe, 2017), where it is thought
433 to be involved in the export of specific tRNA from the nucleus to the cytosol (Grosshans, Lecointe,
434 Grosjean, Hurt, & Simos, 2001). In mammals, PUS1 localizes both to the nuclei and mitochondria
435 (Patton, Bykhovskaya, Mengesha, Bertolotto, & Fischel-Ghodsian, 2005). Our work suggests that
436 PUS1-mediated Ψ has an additional, fundamental function: guiding the export of exRNAs.
437 Knockout of PUS1 in neuronal CADs resulted in a significant loss of Ψ from many RNAs and,
438 importantly, in non-overlapping effects on cellular and extracellular RNA pools (**Fig. 3A–D**). PUS1
439 loss significantly decreased secretion of full-length tRNAs (**Fig. 3F**), likely due to the loss of PUS1-
440 dependent Ψ at position 27 and 28 in the anticodon stem. Interestingly, other Ψ sites remain
441 intact, indicating that modification at these other positions may not be sufficient for export (**Fig.
442 4H–I**) and that the export-related function of Ψ depends on sequence or structural context.

443 **Conclusions and outlook**

444 In conclusion, our screen in neuronal CADs discovered a new pathway for RNA secretion,
445 whereby PUS1 catalyzes the formation of Ψ on select RNAs, marking them for export via EVs,
446 through recognition by MYL6. The genetic identification and biochemical validation of this and
447 other mechanisms governing exRNA selection and transport will enable deeper mechanistic
448 investigation of their downstream biological functions, and, ultimately, help decode the language
449 of RNA-mediated cell-to-cell communication.

450

451 **EXPERIMENTAL PROCEDURES**

452 **Cell culture and conditioned medium collection**

453 CADs (kind gift from S. Berger) (Mews et al., 2017) were maintained in DMEM/F-12 medium
454 (Gibco, Cat. No 11320033) supplemented with 10% ES-grade fetal bovine serum (Gibco, Cat. No
455 16141079), 1% L-Glutamine (Sigma-Aldrich, Cat. No G7513), and 0.5% penicillin/streptomycin
456 solution (Sigma-Aldrich, Cat. No P0781). EV-depleted fetal bovine serum was generated by
457 centrifugation at 100,000 *g* (28,500 rpm) on a SW-32Ti swinging bucket rotor (Beckman Coulter,
458 Cat. No G369650) for 4 h at 4°C, followed by filtration through a 0.22 µm pore size filter (Sigma-
459 Aldrich, Cat. No S2GPU10RE). For EV collection, cells were seeded at 3–15 million per 15-cm
460 dish and washed twice with 1X PBS. Cells were incubated in serum-free medium (same as
461 maintenance medium but without fetal bovine serum) for 48 h (proteomics) or for 24 h (all other
462 analyses) before collecting EVs. For collection of EVs for pooled CRISPR screen (see below),
463 cells were incubated in EV-depleted medium (same as maintenance medium but with EV-
464 depleted fetal bovine serum) for 24 h. To obtain differentiated CADs, cells were maintained in
465 serum-free medium for 5 days.

466 **Extracellular vesicles (EV) isolation and nanoparticle tracking analysis**

467 EV isolation was performed via differential centrifugation, as previously described (Thery et al.,
468 2006) with minor modifications. Briefly, conditioned medium was centrifuged at 300 *g* for 5 min at
469 4°C, followed by centrifugation at 2,000 *g* for 10 min at 4°C and then 10,000 *g* for 30 min at 4°C.
470 Then, the cleared conditioned medium was passed through a 0.22 µm pore size filter (Millipore-
471 Sigma, Cat. No SCGP00525) and centrifuged at 100,000 *g* (28,500 rpm) on a SW-32Ti swinging
472 bucket rotor for 2 h at 4°C. EV pellet was resuspended in 1X PBS and centrifuged again at
473 100,000 *g* (28,500 rpm) on a SW-32Ti swinging bucket rotor for 2 h at 4°C. The washed EV pellet
474 was then resuspended in 100 µL of 1 X PBS and either used immediately or stored at -80°C.

475 For nanoparticle tracking analysis (NTA), EVs were diluted in deionized water and analyzed using
476 the ZetaView PMX220 Twin (Patricle Metrix) with the following parameters: laser wavelength =
477 488 nm; filter wavelength = scatter; shutter = 100; sensitivity = 80. NTA was performed at the
478 extracellular vesicle core at the University of Pennsylvania.

479 **Animals**

480 Male FVB/NJ (8–12 weeks old) were derived from breeders obtained from Jackson Laboratory
481 (Strain #:001800) and maintained in-house. All animal procedures were in strict accordance with

482 the guidelines of the Children's Hospital of Philadelphia and the University of Pennsylvania
483 Institutional Animal Care and Use Committee regulations (CHOP IACUC Protocol #23-001364,
484 UPenn PSOM IACUC Protocol #806911).

485 **Epidydimal tissue and EV collection**

486 Mice were sacrificed by cervical dislocation, and epididymal tissue carefully dissected free of fat
487 and connective tissue. The cauda epididymis was separated and immersed in pre-warmed (37°C)
488 Biggers, Whitten, and Whittingham (BWW) medium (Cafe, Anderson, & Nixon, 2020). Seminal
489 fluid was gently expressed from the tissue. The tissue was removed from the media and flash
490 frozen in a microcentrifuge tube and kept at -80°C until processing for RNA isolation. The released
491 spermatozoa were incubated in BWW medium at 37 °C for 10 min to allow motile sperm to
492 disperse. The suspension was transferred to a fresh microcentrifuge tube and incubated for an
493 additional 10 min at 37 °C to enrich for motile sperm by swim-up. The upper fraction of the
494 suspension was carefully aspirated, leaving ~50 µL of residual medium behind. Spermatozoa
495 were pelleted by centrifugation (10,000 *g*, 5 min), and the supernatant was centrifuged twice at
496 10,000 g for 5 min to remove residual tissue and sperm, each time collecting only the supernatant.
497 A final spin at 10,000 *g* for 30 min at 4 °C was performed to further eliminate debris. The resulting
498 supernatant, containing EVs, was subjected to ultracentrifugation (Optima Max TL, Beckman
499 Coulter) at 120,000 *g* for 2 h at 4 °C. The pellet was washed in 1 mL cold PBS and ultracentrifuged
500 again at 120,000 *g* for 2 h at 4 °C. The final epididymosome pellet was resuspended in 30 µL cold
501 PBS, flash frozen in liquid nitrogen, and stored at -80 °C until RNA isolation.

502 **Cells and EV proteomics**

503 EVs and cells were resuspended in freshly prepared, ice-cold urea lysis buffer (50 mM Tris pH 8,
504 8M urea) and incubated for 1 h at 4°C. Lysates were then sonicated using Bioruptor (Diagenode)
505 with 5 cycles of 30s on / 30 s off and then cleared by centrifugation at 18,000 *g* for 10 min at 4°C.
506 Extract was quantified using the Micro BCA Protein Assay Kit (Thermo Scientific, Cat. No 23235)
507 and 50 µg were taken for further processing. Proteins were prepared using Protifi S-trap Micro
508 columns per manufacturer's instructions. Following S-trap elution, peptides were lyophilized,
509 resuspended in 0.1 % formic acid for further cleanup by desalting. Desalted peptides were
510 lyophilized and resuspended in 4% acetonitrile containing 0.1% formic acid for LC-MS analysis.
511 Mass spectra for peptides were obtained with a Dionex Ultimate3000 liquid chromatograph
512 (Thermo Fisher Scientific) coupled to a Thermo Fusion mass spectrometer (Thermo Fisher
513 Scientific). Peptides were loaded onto an in-house silica capillary column (75 µM inner diameter)

514 packed with C18 resin (ReproSil-Pur C18-AQ 2.4-µm resin; Dr. Maisch GmbH, Ammerbuch,
515 Germany). Peptides were eluted with a gradient of 2%–25% B (86 min) followed by a gradient of
516 25%–50% (32 min) and a hold at 98% B (15 min) (mobile phase A: 0.1% formic acid, mobile
517 phase B: 80% acetonitrile, 0.1% formic acid). Flow rate was 300 nL/min. Data were collected in
518 data-dependent acquisition mode. Full-scan MS settings were as follows: scan range, 300–1,100
519 (m/z; mass-to-charge ratio); resolution, 60,000; AGC, on; micro scan count, 1; Maximum IT, 54
520 ms. MS2 settings were as follows: resolution, 30,000; AGC, predicted; micro scan count, 1;
521 Maximum IT, 100 ms; fragmentation was enforced by higher-energy collisional dissociation with
522 normalized collision energy of 29; isolation width, 1.8 m/z. MS/MS spectra were processed using
523 MetaMorpheus version (https://github.com/smith-chem-wisc/MetaMorpheus) using a UniProt *Mus*
524 *musculus* reference proteome and common contaminants. The following search settings were
525 used: protease = trypsin; search for truncated proteins and proteolysis products = false; maximum
526 missed cleavages = 2; minimum peptide length = 7; maximum peptide length = 60; initiator
527 methionine behavior = variable; fixed modifications = carbamidomethyl on C, carbamidomethyl
528 on U; variable modifications = oxidation on M; max mods per peptide = 1; max modification
529 isoforms = 1,024; precursor mass tolerance = ±10.0000 PPM; product mass tolerance = ±0.0200
530 absolute; report PSM ambiguity = true. Results were filtered for score (> 5) and FDR (1 %).

531 **RNA extraction**

532 Cell pellets or purified EVs were resuspended in 1 mL of TriPure (Roche, Cat. No 11667165001)
533 and RNA was extracted following the recommended protocol. DNA was digested with Turbo
534 DNase-I (Invitrogen, Cat. No AM2238) at 37˚C for 30 min, RNA was re-purified using TriPure and
535 resuspended in modBTE (10mM Bis-Tris pH 6.7, 0.1 mM EDTA). For RNA extraction directly from
536 cleared conditioned medium, 0.3 M NaOAc (final) and 1 volume of phenol-chloroform-IAA
537 (Ambion, Cat. No AM9732) were added and RNA was purified using the recommended protocol.
538 DNA was digested and RNA was re-purified using TriPure as described above.

539 **LIDAR, small RNA-seq, and mRNA-seq libraries**

540 LIDAR libraries from 100–250 ng of cellular RNA or 1–50 ng of EV RNA were prepared as
541 described (Scacchetti et al., 2024) with some minor modification. LIDAR_RT_primer and
542 LIDAR_TSO_mix were diluted 1:3 for samples where RNA input was < 10 ng. Reverse
543 transcription conditions were changed to the following: 8°C for 10 min, 16°C for 10 min, 25°C for
544 10 min, 42°C for 80 min, 10 cycles at 50˚C for 2 min and 42˚C for 2 min, 85°C for 5 min. Lastly,
545 the amount of indexing primers was increased to 10 pmol. LIDAR libraries were analyzed on a

546 2% agarose gel and quantified using Qubit dsDNA Quantification Assay kit (Invitrogen, Cat. No
547 Q32854).

548 Small RNA libraries were prepared using the NEBnext small RNA library kit for Illumina (New
549 England Biolabs, Cat. No E7330S), following the standard protocol with the following parameters:
550 1) 1:2 dilution of 3'SR Adaptor, SR RT Primer, and 5'SR Adaptor, 2) 15 indexing PCR cycles, 3)
551 cleanup of final libraries with QIAgen MinElute PCR purification kit (QIAgen, Cat. No 28004),
552 followed by a second cleanup with 2X SPRI. Libraries were analyzed on 6% non-denaturing
553 polyacrylamide gels.

554 Conventional mRNA-seq libraries were prepared from 2 µg of total CAD RNA following the
555 protocol described in (Scacchetti et al., 2024).

556 Libraries were sequenced on Illumina NextSeq1000 or NextSeq2000 instruments.

557 **Genome-wide pooled CRISPR-Cas9 screen**

558 The mouse Brie sgRNA library (Doench et al., 2016) in the lentiCRISPR v2 and lentiGuide-Puro
559 backbones were obtained from Addgene (Cat. No 73632 and 73632). The library were amplified
560 in ElectroMAX Stbl4 competent cells (Invitrogen, Cat. No 11635018). To generate lentiviruses,
561 ~100 million HEK293FT were transfected with 275 µg of amplified library together with 170 µg of
562 psPAX2 packaging plasmid (Addgene, Cat. No 12260) and 96 µg of pMDG.2 envelope plasmid
563 (Addgene, Cat. No 12259) using Lipofectamine 3000 Transfection Reagent (Invitrogen, Cat. No
564 L3000015). 18 h after transfection, the medium was changed to lentivirus_collection_medium
565 [DMEM high glucose (Gibco, Cat. No 11965126) supplemented with 10% ES-grade fetal bovine
566 serum (Gibco, Cat. No 16141079), 1% GlutaMAX (Gibco, Cat. No 35050061), 1% MEM non-
567 essential amino acid solution (Sigma-Aldrich, Cat. No M7145-100ML), 1% sodium pyruvate
568 (Millipore-Sigma, Cat. No S8636), and 1% bovine serum albumin (Sigma-Aldrich, Cat. No A1933).
569 Conditioned medium was collected 48 h later, filtered through a 0.45 µm filter (Millipore-Sigma,
570 Cat. No S2HVU11RE), and concentrated using Amicon Ultra centrifugal filters with 100 kDa
571 MWCO (Millipore-Sigma, Cat. No UFC910008). Concentrated lentiviruses were aliquoted and
572 stored at -80°C. Multiplicity of infection (MOI) in CADs was estimated as described (Shalem et
573 al., 2014). Briefly, CADs were infected with increasing amounts of lentivirus using 8 µg/mL
574 polybrene (final concentration). 24 h after infection, cells were divided equally into two new wells
575 and one of them was treated with 1 µg/mL puromycin (Invivogen, Cat. No ant-pr-1). 96 h later,
576 cells were counted, and the MOI was determined as the percentage of surviving cells. To test for
577 sgRNA presence in EV preparations, CADs were infected with the Brie lentiGuide-Puro (sgRNA

578 only) libraries at an MOI of 0.43 and ~1X coverage, selected with 1 µg/ml puromycin for 7 days,
579 and stably transduced cells were frozen in liquid N_2. RT-qPCR for sgRNA expression was
580 performed using Power SYBR Green RNA-to-C_T (Applied Biosystems, Cat. No 4389986) with the
581 sgRNA_1_qPCR primers (**Table S5**).

582 The genome-wide screen was performed in 2 biological replicates. 55 million CADs were
583 transduced on day 0 with the lentiviral library at an MOI of 0.21 using 8 µg/mL polybrene to result
584 in ~100-150X sgRNA coverage. 24 h after infection, cells were washed twice with PBS and EV-
585 depleted medium was added. 24 h later ("day 2" throughout the manuscript), EVs and half the
586 cells were collected as described above and resuspended in TriPure. The other half of the cells
587 was re-plated with maintenance media containing 1 µg/mL puromycin. Cells were selected with
588 puromycin for 7 days. Then, cells were washed twice with PBS and EV-depleted medium was
589 added. 24 h later ("day 10" throughout the manuscript), EVs and cells were collected once again
590 and resuspended in TriPure. RNA was extracted from all samples as described. For cell samples,
591 < 200 nts RNAs were enriched using Zymo RNA Clean & Concentrator – 25 (Zymo Research,
592 Cat. No. R1017) following the recommended protocol.

593 sgRNA-seq libraries were prepared using a modified LIDAR protocol starting from half of the total
594 amount of RNA obtained from cells and EVs. In the case of cells, multiple parallel libraries were
595 prepared to not exceed 1.5 µg of input RNA / library, which were then pooled before sequencing.
596 Briefly, RNAs was diluted to 2.8 µL and mixed with 0.4 µL of 10 µM LIDAR_sgRNA_RT_primer
597 (see **Table S5** for all oligonucleotide sequences). Samples were heated to 70˚C for 2 min, then
598 cooled to 4˚C (0.5˚C/s). Next, 4.8 µL of RT_mix [25 mM Tris-HCl pH 8.3, 20 mM NaCl, 2.5 mM
599 $MgCl_2$, 8 mM DTT, 5% PEG-8000, 0.5 mM dNTPs, 1 mM GTP, 0.32 µL of 50 µM LIDAR_TSO
600 mix (Scacchetti et al., 2024) or SS3_TSO, 0.5 U/µL murine RNase inhibitor (New England Biolabs,
601 Cat. No M0314S), and 2U/µL Maxima H-minus RT (Thermo Scientific, Cat. No EP0752);
602 concentrations refer to a final volume of 8 µL] were added. Reverse transcription was performed
603 as follows: 42°C for 90 min, 10 cycles at 50˚C for 2 min and 42˚C for 2 min, 85°C for 5 min. cDNA
604 was pre-ampified by adding 12 µL of KAPA_mix [1X KAPA HiFi HotStart buffer Ready Mix (Roche,
605 Cat. No KK2601), 1 µM LIDAR_preamp_f, and 0.1 µM LIDAR_preamp_r (Scacchetti et al., 2024);
606 concentrations refer to a final volume of 20 µL] and by following these PCR cycling conditions:
607 denaturation (95˚C for 3 min), 5 x (98˚C for 20 s, 70˚C for 30 s, 72˚C for 30 s), final extension
608 (72˚C for 5 min). Pre-amplified libraries were purified using 2.5X SPRI beads (Beckman Coulter,
609 Cat. No B23319) and eluted in 37 µL of TE buffer (10mM Tris-HCl pH 8, 1 mM EDTA). 0.5 µL of
610 each 10 µM custom Nextera indexing primers was added, followed by 12 µL of Q5_mix [1X Q5

611 buffer, 0.5 mM dNTPs, 0.02 U/µL Q5 High-Fidelity DNA Polymerase (New England Biolabs, Cat.
612 No M0491); concentrations refer to a final volume of 50 µL]. Samples were incubated with the
613 following PCR cycling conditions: denaturation (98˚C for 30 s), 15 x (98˚C for 10 s, 65˚C for 20 s,
614 72˚C for 20 s). Final libraries were purified using 2X SPRI beads (Beckman Coulter, Cat. No
615 B23319) and eluted in 45 µL of TE buffer (10 mM Tris-HCl pH 8, 1 mM EDTA). Libraries were
616 analyzed on a 2% agarose gel and quantified using Qubit dsDNA Quantification Assay kit
617 (Invitrogen, Cat. No Q32854). Libraries were sequenced on Illumina NextSeq500, NextSeq1000,
618 or NextSeq2000 instruments.

619 **CRISPRi**

620 CRISPRi sgRNAs targeting the promoter region of *Sdcbp*, *Pus1,* and control (see **Table S5** for
621 all oligonucleotide sequences) were cloned in Lenti-(BB)-EF1a-KRAB-dCas9-P2A-BlastR
622 (Addgene, Cat. No 118154) using Golden Gate. To generate lentiviruses, ~0.5 million HEK293FT
623 in 6-well plates were transfected with 1.5 µg of CRISPRi plasmid together with 1 µg of psPAX2
624 packaging plasmid (Addgene, Cat. No 12260) and 0.5 µg of pMDG.2 envelope plasmid (Addgene,
625 Cat. No 12259) using Lipofectamine 3000 Transfection Reagent (Invitrogen, Cat. No L3000015).
626 24 h after transfection, medium was changed to lentivirus_collection_medium. Conditioned
627 medium was collected 48 h later, and cell and debris were removed by centrifugation at 500 *g* for
628 5 min, followed by 1,250 *g* for 5 min. Cleared conditioned medium containing lentivirus was
629 concentrated to 50 µL using Amicon Ultra Centrifugal Filter with 100 kDa MWCO (Millipore-Sigma,
630 Cat. No UFC5100). To generate stable CRISPRi cells, 50 thousand CADs were transduced with
631 50 µL of lentiviruses using 8 µg/mL polybrene (final concentration). 48 h after infection, medium
632 was supplemented with with 20 µg/mL blasticidin (Invivogen, Cat. No ant-bl-1) and cells were
633 selected for 4 days. To generate the pool of different CRISPRi cells, approximately equal number
634 of cells from individual knockdowns were mixed and cells were expanded in the presence of 20
635 µg/mL blasticidin. Cells were washed twice with PBS and EV-depleted medium was added. 24 h
636 later, conditioned medium was collected and cleared at 300 *g* for 5 min at 4°C, followed by
637 centrifugation at 2,000 *g* for 10 min at 4°C, 10,000 *g* for 30 min at 4°C, and concentration using
638 Amicon Ultra Centrifugal Filter with 100 kDa MWCO (Millipore-Sigma, Cat. No UFC5100). RNA
639 was extracted from cells and concentrated conditioned medium as described above. sgRNA-seq
640 libraries were prepared as described for the genome-wide screen using LIDAR_TSO_mix during
641 the reverse transcription. Libraries were sequenced on Illumina NextSeq1000 or NextSeq2000
642 instruments.

643 **Generation of *Sdcbp*$^{-/-}$ and *Pus1*$^{-/-}$ cells**

644 sgRNAs targeting *Sdcbp* and *Pus1* (see **Table S5** for all oligonucleotide sequences) were cloned
645 in PX459 (Addgene, Cat. No 62988) using Golden Gate. 0.5 million CADs were transfected with
646 2.5 µg of the targeting plasmids (PX459 backbone) using Lipofectamine 3000 Transfection
647 Reagent (Invitrogen, Cat. No L3000015). 24 h after transfection, medium was supplemented with
648 2 µg/mL puromycin, and cells were selected for 48 h. Next, cells were seeded in 15-cm dishes at
649 500–1,000 cells per dish and incubated for 6 days without puromycin. Individual colonies
650 (corresponding to single clonal populations) were picked and transferred to 96-well plates. Clones
651 were expanded and tested by western blot to assess knock-out efficiency. Whole cell extracts
652 were prepared by lysis of cell pellets in RIPA buffer (10 mM Tris-HCl pH 8, 140 mM NaCl, 1 mM
653 EDTA, 0.1% Na-deoxycholate, 1% Triton-X-100, 0.1% SDS, 1X cOmplete EDTA-free Protease
654 Inhibitor), followed by sonication using Bioruptor (Diagenode) (30 s ON/OFF, 5 cycles) and
655 clarification by centrifugation at 18,000 *g* for 10 min at 4°C.The following antibody dilutions were
656 used for western blots: 1:1000 for αSDCBP (Abcam, Cat. No ab19903), 1:500 for αPUS1 (Abcam,
657 Cat. No ab203010), 1:1000 for αSUZ12 (Cell Signaling Technology, Cat. No 3737S), 1:1000 for
658 αTUBB (Abcam, Cat. No ab6046).

659 **Export of synthetic sgRNAs**

660 sgRNAs containing uridine or pseudouridine (Ψ) were synthesized by *in vitro* transcription. Briefly,
661 individual sgRNAs were PCR amplified to add a sense T7 promoter sequence (**Table S5**). RNA
662 was transcribed from ~500 ng of template DNA using HiScribe T7 High Yield RNA Synthesis Kit
663 (New England Biolabs, Cat. No E2040L) following the recommended protocol for short RNAs.
664 UTP was substituted with pseudo-UTP (Jena Bioscience, Cat. No NU-1139L) to generate Ψ-
665 containing sgRNAs. DNA was digested with Turbo DNase-I (Invitrogen, Cat. No AM2238) and
666 RNA was purified using TriPure (Roche, Cat. No 11667165001) as described above.

667 For assessing export with qPCR, 0.2 million CADs were transfected with 1 µg of UTP- or Ψ-
668 containing EGFP_1_sgRNA using Lipofectamine RNAiMAX Transfection Reagent (Invitrogen,
669 Cat. No 13778075). 6 h after transfection, cells were washed with serum-free medium, and then
670 incubated for additional 20 h in serum-free medium. Conditioned medium was collected and
671 cleared at 300 *g* for 5 min at 4°C, followed by centrifugation at 2,000 *g* for 10 min at 4°C and then
672 10,000 *g* for 30 min at 4°C. RNA was extracted from cells and cleared conditioned medium as
673 described above. RT-qPCR was performed using Power SYBR Green RNA-to-C_T (Applied
674 Biosystems, Cat. No 4389986) with the EGFP_1_qPCR primers (**Table S5**). For assessing export

675 by sequencing, the same procedure was followed with some minor modifications. First, two
676 different sgRNA pools were created mixing 3 UTP-containing and 3 Ψ-containing sgRNAs (**Table**
677 **S5**). Second, 500 ng of sgRNA pools were used to transfect 0.3 million CADs. RNA was extracted
678 from cells and cleared conditioned medium as described above. sgRNA-seq libraries were
679 prepared using the same strategy as in the genome-wide screen. Libraries were sequenced on
680 Illumina NextSeq1000 or NextSeq2000 instruments.

681 **Bisulfite-modified LIDAR**

682 Bisulfite conversion and desulphonation of RNA was performed following the BID-seq protocol
683 (Dai et al., 2023). Briefly, input RNA (200 ng for cellular RNA and 10 ng for exRNAs) was diluted
684 in 8.5 µL of water, 45 µL of freshly prepared BS reagent (2.4 M Na_2SO_3 and 0.36 M $NaHSO_3$)
685 were added, and samples were incubated at 70°C for 3 h. Next, 75 µL of water, 270 µL of RNA
686 Binding Buffer (Zymo Research, Cat. No. R1013), and 400 µL of 100% EtOH were added, and
687 samples were transferred on a Zymo column (Zymo Research, Cat. No. R1013). After washing
688 with 200 µL of RNA wash buffer, samples were incubated in-column with 200 µL of RNA
689 desulphonation buffer (Zymo Research, Cat. No. R5001-3-40) for 1 h and 15 min at 25°C.
690 Samples were washed with twice with RNA wash buffer (400 µL and 700 µL), then eluted in 6 µL
691 of RNase-free water. Libraries were prepared starting from half of the eluate using the LIDAR
692 protocol described above with a few modifications: 1) initial RNA denaturation was conducted at
693 72°C for 3 min; 2) $MgCl_2$ was substituted with $MnCl_2$ in the RT_mix (keeping the same amounts);
694 3) reverse transcription conditions were changed to 8°C for 10 min, 16°C for 10 min, 25°C for 10
695 min, 42°C for 80 min, 10 cycles at 50˚C for 2 min and 42˚C for 2 min, 85°C for 5 min. Libraries
696 from untreated RNA input samples were prepared in parallel.

697 **RNA affinity chromatography**

698 Biotinylated sgRNAs containing U or Ψ were generated by *in vitro* transcription. Individual
699 sgRNAs were PCR amplified to add a sense T7 promoter sequence (**Table S5**). RNA was
700 transcribed from ~600 ng of template DNA (1:1 mix of EGFP_1_sgRNA and SCR_1_sgRNA)
701 using HiScribe T7 High Yield RNA Synthesis Kit (New England Biolabs, Cat. No E2040L) following
702 the recommended protocol for short RNAs. In all reactions, ATP was substitute with a 10:1 mix of
703 ATP and N6-(6-Aminohexyl)-ATP-Biotin (Jena Bioscience, Cat. No NU-805-BIO). UTP was
704 substituted with pseudo-UTP (Jena Bioscience, Cat. No NU-1139L) to generate Ψ-containing
705 sgRNAs. DNA was digested with Turbo DNase-I (Invitrogen, Cat. No AM2238) and RNA was
706 purified using TriPure (Roche, Cat. No 11667165001) as described above.

707 To prepare protein extracts, approximately 50 million CADs were collected and washed with PBS.
708 Cell pellets were resuspended in 1 mL of ice-cold CHAPS lysis buffer [50 mM Tris-Cl pH = 7.5,
709 150 mM NaCl, 0.5% CHAPS, 0.5 mM DTT, 1 X cOmplete EDTA-free Protease Inhibitor Cocktail
710 (Roche, Cat. No 11873580001)] and cells were lysed via 2 cycles of freezing in dry ice/EtOH bath
711 followed by rapid thawing at 37°C. Extract was clarified by centrifugation at 18,000 *g* for 10 min
712 at 4°C. Protein amounts were quantified using Bio-Rad Protein Assay Dye Reagent Concentrate
713 (Bio-Rad, Cat. No 5000006).

714 50 µg of U- or Ψ-containing biotinylated sgRNAs were mixed with 1 mg of CAD protein extract in
715 CHAPS lysis buffer supplemented with 1.5 mM $MgCl_2$ and the samples were rotated for 1 h at
716 room temperature. As a control, RNA was omitted from 1 reaction ("beads only"). Next, 50 µL of
717 Dynabeads MyOne Streptavidin C1 beads (Invitrogen, Cat. No 65001), equilibrated in CHAPS
718 lysis buffer supplemented with 1.5 mM $MgCl_2$, were added and samples were rotated for 1 h at
719 4°C. Beads were washed 3 X with medium salt buffer (50 mM Tris-Cl pH = 7.5, 150 mM NaCl,
720 1.5 mM $MgCl_2$, 0.5 mM DTT, 1 X cOmplete EDTA-free Protease Inhibitor Cocktail) and 3 X with
721 high salt buffer (50 mM Tris-Cl pH = 7.5, 500 mM NaCl, 1.5 mM $MgCl_2$, 0.5 mM DTT, 1 X cOmplete
722 EDTA-free Protease Inhibitor Cocktail). Proteins were prepared using Protifi S-trap Micro columns
723 per manufacturer's instructions. Following S-trap elution, peptides were lyophilized, resuspended
724 in 0.1 % formic acid for further cleanup by desalting. Desalted peptides were lyophilized and
725 resuspended in 4% acetonitrile containing 0.1% formic acid for LC-MS analysis. Mass spectra for
726 peptides were obtained with a Dionex Ultimate3000 liquid chromatograph (Thermo Fisher
727 Scientific) coupled to a Q-Exactive HF mass spectrometer (Thermo Fisher Scientific). Peptides
728 were loaded onto an in-house silica capillary column (75 µM inner diameter) packed with C18
729 resin (ReproSil-Pur C18-AQ 2.4-µm resin; Dr. Maisch GmbH, Ammerbuch, Germany). Peptides
730 were eluted with a gradient of 2%–25% B (85 min) followed by a gradient of 25%–50% (30 min)
731 and a hold at 98% B (15 min) (mobile phase A: 0.1% formic acid, mobile phase B: 80%
732 acetonitrile, 0.1% formic acid). Flow rate was 300 nL/min. Data were collected in data-
733 independent acquisition (DIA) mode had the following settings: Full scan MS – Scan range, 385–
734 1015 m/z; AGC target, 1e6; Ion inject time, 60 ms; Resolution, 60,000; Isolation width, 630.
735 MS/MS scan – Resolution, 30,000; MS2 AGC target, 1e6, Ion inject time, 60 ms; Isolation width,
736 24; HCD energy, 30. The reference proteomes used for data processing were the Uniprot Mus
737 musculus reference proteome and a Cas9 FASTA (UniprotID: Q99ZW2). DDA spectra were
738 processed with ProteomeDiscoverer (version 2.4.1.15) and Sequest. False discovery rates (FDR)
739 were estimated using a decoy database search with strict and relaxed target FDRs set to 0.01
740 and 0.05, respectively. DIA spectra were processed with DIA-NN (version 1.9.2). Outputs were

741 filtered at 0.01 FDR, which were estimated based on in silico-generated spectral libraries
742 generated by DIA-NN.

743 ***Myl6* knock-down**

744 siRNAs against *Myl6* and TYE 563 Control DsiRNA were obtained from Integrated DNA
745 Technologies (Cat. No mm.Ri.Myl6.13.2, and TriFECTa RNAi Kit). CADs were transfected with
746 siRNAs using Lipofectamine RNAiMAX using 15 pmol of siRNA per 0.3 million cells. Knockdown
747 efficiency was measured 72 h after transfection via RT-qPCR using Power SYBR Green RNA-to-
748 C_T (Applied Biosystems, Cat. No 4389986) with the Myl6_qPCR primers (**Table S5**).

749 **DATA PROCESSING AND ANALYSIS**

750 **Proteomics data processing and analysis**

751 Protein with measurable intensities only in cell or only in EV samples were excluded from the plot
752 in **Fig. 1C** and denoted as "Cell-exclusive" or "EV-exclusive" in **Table S1**. Raw intensities were
753 normalized using the `median_normalization` function or `proDA` package (Ahlmann-Eltze &
754 Anders, 2020). Differential abundance analysis was performed in R using the `limma` package as
755 previously described (Kammers, Cole, Tiengwe, & Ruczinski, 2015; Ritchie et al., 2015). Adjusted
756 *p* values (FDR) were calculated using the `p.adjust` function (method = 'fdr'*)*. Gene ontology
757 analysis was performed using DAVID (Cellular component 5) (Huang, Sherman, & Lempicki,
758 2008; Sherman et al., 2022), including "EV-exclusive" proteins.

759 **Processing, mapping, and read counting (LIDAR, BID-LIDAR, small RNA-seq, mRNA-seq)**

760 Adapter trimming, UMI extraction, mapping to the *M. musculus* genome , deduplication and read
761 counting for LIDAR, BID-LIDAR, and small RNA-seq (NEB) was performed exactly as described
762 in (Scacchetti et al., 2024) with scripts available on GitHub (https://github.com/bonasio-lab). For
763 mRNA-seq libraries, paired-end reads were mapped directly using STAR (Dobin et al., 2013) with
764 the following parameters: `--peOverlapNbasesMin 10 --readMapNumber -1 --`
765 `clip3pNbases 0 --alignIntronMax 100000 --outSAMtype BAM Unsorted`. Counts
766 per gene were calculated in R using summarizeOverlaps function from GenomicAlignments.
767 RNAs with 0 counts in all wild type samples (cellular or exRNAs) were excluded. Raw counts
768 were batch corrected using `Combat_seq` (Zhang, Parmigiani, & Johnson, 2020).

769 **Processing, mapping and, read counting (sgRNA libraries)**

770 Adapter trimming on single-end reads was performed using `Cutadapt` (Martin, 2011) with the
771 following parameters: `-a gttttagagcta -m 6`. UMI extraction was performed using the
772 `process_files_single.sh` script available on GitHub (https://github.com/bonasio-lab) with
773 the following parameters: 8bp (libraries constructed using SS3_TSO) or LIDAR (libraries
774 constructed using LIDAR_TSO_mix). Reads were further trimmed with `Cutadapt` with the
775 following parameter: `-u 1`. Reads were mapped to the reference sgRNA Brie library or the sgRNA
776 sequences used in "Export of synthetic sgRNAs" using `bowtie2` (Langmead & Salzberg, 2012)
777 using standard parameters but specifying `--no-rc`. Aligned reads were deduplicated using
778 `umi_tools` (Smith, Heger, & Sudbery, 2017) with the following parameter: `--method unique`.
779 Reads shorter than 15 bp were filtered out using `bedtools` (Quinlan, 2014). Read counting was
780 performed from bam files using MAGeCK (W. Li et al., 2014) with the following parameters:
781 `count`. Raw counts were batch corrected using `Combat_seq` (Zhang et al., 2020).

782 **CRISPR screen analysis**

783 Batch corrected raw counts were normalized using MAGeCK with the following parameter: `count`
784 `-norm-method total`. Differential sgRNA abundance between cell and EVs at day 2 was
785 calculated with DESeq2 (Love, Huber, & Anders, 2014) with the following parameter: `fitType`
786 `= "local"`.

787 To identify candidates, first sgRNAs targeting genes not expressed in CADs (RPKM <1) were
788 excluded. Then, to account for individual sgRNA export efficiency as well as changes in sgRNA
789 representation in cells at day 10 due to fitness effects, we calculated a "predicted" sgRNA
790 abundance in day 10 EVs as follows:

791 $$i_{EV(day10)predicted} = average\left(\frac{i_{EV(day2)observed}}{i_{Cells(day2)observed}}\right) \times i_{Cells(day10)observed}$$

792 Where i is the sgRNA read frequency in the indicated samples. Differences in EV sgRNA
793 predicted and observed abundance at day 10 were calculated using MAGeCK with the following
794 parameter: `test -paired`. GO analysis was performed using DAVID (cellular component, GO
795 level #5) (Huang et al., 2008; Sherman et al., 2022).

796 **Differential RNA abundance analysis (LIDAR)**

797 Differential abundance between wild type cellular and exRNAs, as well as comparisons between
798 wild type and *Pus1*$^{-/-}$ mutant CAD, was performed using DESeq2 (Love et al., 2014) with the

following parameter: `fitType = "local"`. RNAs with an adjusted *p* value < 0.1 were considered differentially enriched/exported.

Analysis of Ψ with BID-LIDAR

Detection of genomic positions with Ψ was done by identifying positions with deletions induced by BID sequencing compared to a non-bisulfite-induced input. First, reads were mapped using the LIDAR analysis pipeline, as described ab An in-house script using `GenomicRanges` (Lawrence et al., 2013), `BioStrings` (https://bioconductor.org/packages/release/bioc/html/Biostrings.html), and `bedtools` (Quinlan, 2014) was used to detect deletions within reads, map putative Ψ sites to the genome reference, and calculate the fraction of reads at each genomic position that contain a deletion. Only positions with at least 5% of reads deleted were considered to harbor a deletion. Positions where deletion occurred 2 X more frequently in BID than input samples were classified as Ψ sites. Position with a BID deletion rate in wild type < 0.75X compared to *Pus1*$^{-/-}$ were classified as PUS1-sensitive Ψ sites. These positions were then assigned to the transcripts that contained them to generate a list of modified RNAs.

For tRNA analysis of BID-LIDAR, the position of canonical bases for each tRNA gene were annotated using the strategy described in (Scacchetti et al., 2024). These positions were used to identify tRNA containing a U at position 27, which served as candidates for containing a Ψ at this position, and to visualize and quantify reads with deletions at each canonical base.

DATA AVAILABILITY

Sequencing data will be deposited in GEO upon restoration of NCBI services.

Proteomics data deposited at PRIDE: PXD069544 and PXD069598

Code will be available on GitHub

ACKNOWLEDGMENTS

The authors thank Andy J. Minn for technical advice, and Kenneth Zaret and the Bonasio lab for feedback on the experiments and manuscript. R.B. acknowledges support from the NIH (R35GM153281; DP1NS148061). C.C.C. acknowledges support from the NIH (R35GM151087) This project was supported in part by a Penn Epigenetics Institute Pilot grant to R.B. and A.S.

827 **AUTHOR CONTRIBUTIONS**

828 Conceptualization: A.S. and R.B.; methodology: A.S., E.J.S., R.B. ; formal analyses: A.S., E.J.S.,
829 R.B.; investigation: A.S., E.J.S., L.N.R, J.F.D, J.T., G.E.L., R.L., N.C. ; data curation: A.S., E.J.S.,
830 R.B.; writing – original draft: A.S. and R.B.; writing – review & editing: all authors; visualization:
831 A.S., E.J.S., R.B.; supervision: R.B., C.C.C., N.C., B.A.G.; project administration: A.S. and R.B.;
832 funding acquisition: R.B.

833 **DECLARATION OF INTEREST**

834 The authors declare no competing interest.

835 **REFERENCES**

836 Ahlmann-Eltze, C., & Anders, S. (2020). proDA: Probabilistic Dropout Analysis for Identifying
837 Differentially Abundant Proteins in Label-Free Mass Spectrometry. *bioRxiv*.
838 doi:10.1101/661496

839 Al Othman, A., Bagrov, D., Rozenberg, J. M., Glazova, O., Skryabin, G., Tchevkina, E., . . .
840 Durymanov, M. (2024). Retrovirus-like gag protein Arc/Arg3.1 is involved in extracellular-
841 vesicle-mediated mRNA transfer between glioma cells. *Biochim Biophys Acta Gen Subj,*
842 *1868*(1), 130522. doi:10.1016/j.bbagen.2023.130522

843 Ashley, J., Cordy, B., Lucia, D., Fradkin, L. G., Budnik, V., & Thomson, T. (2018). Retrovirus-like
844 Gag Protein Arc1 Binds RNA and Traffics across Synaptic Boutons. *Cell, 172*(1-2), 262-
845 274 e211. doi:10.1016/j.cell.2017.12.022

846 Baietti, M. F., Zhang, Z., Mortier, E., Melchior, A., Degeest, G., Geeraerts, A., . . . David, G. (2012).
847 Syndecan-syntenin-ALIX regulates the biogenesis of exosomes. *Nature cell biology,*
848 *14*(7), 677-685. doi:10.1038/ncb2502

849 Barman, B., Sung, B. H., Krystofiak, E., Ping, J., Ramirez, M., Millis, B., . . . Weaver, A. M. (2022).
850 VAP-A and its binding partner CERT drive biogenesis of RNA-containing extracellular
851 vesicles at ER membrane contact sites. *Dev Cell, 57*(8), 974-994 e978.
852 doi:10.1016/j.devcel.2022.03.012

853 Bellingham, S. A., Coleman, B. M., & Hill, A. F. (2012). Small RNA deep sequencing reveals a
854 distinct miRNA signature released in exosomes from prion-infected neuronal cells. *Nucleic*
855 *Acids Res, 40*(21), 10937-10949. doi:10.1093/nar/gks832

856 Bervoets, S., Jacob, M. S., Devineni, A. V., Mahoney, B. D., Sullivan, K. R., Butts, A. R., . . .
857 Caron, S. J. C. (2024). dArc1 controls sugar reward valuation in Drosophila melanogaster.
858 *bioRxiv*. doi:10.1101/2024.11.04.621761

Betti, F., Ladera-Carmona, M. J., Weits, D. A., Ferri, G., Iacopino, S., Novi, G., . . . Perata, P. (2021). Exogenous miRNAs induce post-transcriptional gene silencing in plants. *Nat Plants, 7*(10), 1379-1388. doi:10.1038/s41477-021-01005-w

Blanchette, C. R., Scalera, A. L., Harris, K. P., Zhao, Z., Dresselhaus, E. C., Koles, K., . . . Rodal, A. A. (2022). Local regulation of extracellular vesicle traffic by the synaptic endocytic machinery. *J Cell Biol, 221*(5). doi:10.1083/jcb.202112094

Brito, C., & Sousa, S. (2020). Non-Muscle Myosin 2A (NM2A): Structure, Regulation and Function. *Cells, 9*(7). doi:10.3390/cells9071590

Budnik, V., Ruiz-Canada, C., & Wendler, F. (2016). Extracellular vesicles round off communication in the nervous system. *Nat Rev Neurosci, 17*(3), 160-172. doi:10.1038/nrn.2015.29

Cafe, S. L., Anderson, A. L., & Nixon, B. (2020). In vitro Induction and Detection of Acrosomal Exocytosis in Human Spermatozoa. *Bio Protoc, 10*(14), e3689. doi:10.21769/BioProtoc.3689

Cai, Q., Qiao, L., Wang, M., He, B., Lin, F. M., Palmquist, J., . . . Jin, H. (2018). Plants send small RNAs in extracellular vesicles to fungal pathogen to silence virulence genes. *Science, 360*(6393), 1126-1129. doi:10.1126/science.aar4142

Caohuy, H., & Pollard, H. B. (2002). Protein kinase C and guanosine triphosphate combine to potentiate calcium-dependent membrane fusion driven by annexin 7. *J Biol Chem, 277*(28), 25217-25225. doi:10.1074/jbc.M202452200

Caudron-Herger, M., Jansen, R. E., Wassmer, E., & Diederichs, S. (2021). RBP2GO: a comprehensive pan-species database on RNA-binding proteins, their interactions and functions. *Nucleic Acids Res, 49*(D1), D425-D436. doi:10.1093/nar/gkaa1040

Caudron-Herger, M., Rusin, S. F., Adamo, M. E., Seiler, J., Schmid, V. K., Barreau, E., . . . Diederichs, S. (2019). R-DeeP: Proteome-wide and Quantitative Identification of RNA-Dependent Proteins by Density Gradient Ultracentrifugation. *Mol Cell, 75*(1), 184-199 e110. doi:10.1016/j.molcel.2019.04.018

Cerneckis, J., Cui, Q., He, C., Yi, C., & Shi, Y. (2022). Decoding pseudouridine: an emerging target for therapeutic development. *Trends Pharmacol Sci, 43*(6), 522-535. doi:10.1016/j.tips.2022.03.008

Cha, D. J., Franklin, J. L., Dou, Y., Liu, Q., Higginbotham, J. N., Demory Beckler, M., . . . Patton, J. G. (2015). KRAS-dependent sorting of miRNA to exosomes. *Elife, 4*, e07197. doi:10.7554/eLife.07197

Chen, Z., Zhou, Y., Xue, C., Zeng, L., Deng, S., Xu, Z., . . . Zheng, J. (2025). Psychological stress-induced ALKBH5 deficiency promotes tumour innervation and pancreatic cancer via extracellular vesicle transfer of RNA. *Nat Cell Biol, 27*(6), 1035-1047. doi:10.1038/s41556-025-01667-0

Chevillet, J. R., Kang, Q., Ruf, I. K., Briggs, H. A., Vojtech, L. N., Hughes, S. M., . . . Tewari, M. (2014). Quantitative and stoichiometric analysis of the microRNA content of exosomes. *Proc Natl Acad Sci U S A, 111*(41), 14888-14893. doi:10.1073/pnas.1408301111

Chitti, S. V., Gummadi, S., Kang, T., Shahi, S., Marzan, A. L., Nedeva, C., . . . Mathivanan, S. (2024). Vesiclepedia 2024: an extracellular vesicles and extracellular particles repository. *Nucleic Acids Res, 52*(D1), D1694-D1698. doi:10.1093/nar/gkad1007

Conibear, E., Cleck, J. N., & Stevens, T. H. (2003). Vps51p mediates the association of the GARP (Vps52/53/54) complex with the late Golgi t-SNARE Tlg1p. *Mol Biol Cell, 14*(4), 1610-1623. doi:10.1091/mbc.e02-10-0654

Conine, C. C., & Rando, O. J. (2022). Soma-to-germline RNA communication. *Nat Rev Genet, 23*(2), 73-88. doi:10.1038/s41576-021-00412-1

Costa, B., Li Calzi, M., Castellano, M., Blanco, V., Cuevasanta, E., Litvan, I., . . . Tosar, J. P. (2023). Nicked tRNAs are stable reservoirs of tRNA halves in cells and biofluids. *Proc Natl Acad Sci U S A, 120*(4), e2216330120. doi:10.1073/pnas.2216330120

Crocker, O. J., Trigg, N. A., & Conine, C. C. (2022). Cloning and Sequencing Eukaryotic Small RNAs. *Curr Protoc, 2*(8), e495. doi:10.1002/cpz1.495

Dai, Q., Zhang, L. S., Sun, H. L., Pajdzik, K., Yang, L., Ye, C., . . . He, C. (2023). Quantitative sequencing using BID-seq uncovers abundant pseudouridines in mammalian mRNA at base resolution. *Nat Biotechnol, 41*(3), 344-354. doi:10.1038/s41587-022-01505-w

Deatherage, B. L., & Cookson, B. T. (2012). Membrane vesicle release in bacteria, eukaryotes, and archaea: a conserved yet underappreciated aspect of microbial life. *Infect Immun, 80*(6), 1948-1957. doi:10.1128/IAI.06014-11

Dixson, A. C., Dawson, T. R., Di Vizio, D., & Weaver, A. M. (2023). Context-specific regulation of extracellular vesicle biogenesis and cargo selection. *Nat Rev Mol Cell Biol, 24*(7), 454-476. doi:10.1038/s41580-023-00576-0

Dobin, A., Davis, C. A., Schlesinger, F., Drenkow, J., Zaleski, C., Jha, S., . . . Gingeras, T. R. (2013). STAR: ultrafast universal RNA-seq aligner. *Bioinformatics, 29*(1), 15-21. doi:10.1093/bioinformatics/bts635

Doench, J. G., Fusi, N., Sullender, M., Hegde, M., Vaimberg, E. W., Donovan, K. F., . . . Root, D. E. (2016). Optimized sgRNA design to maximize activity and minimize off-target effects of CRISPR-Cas9. *Nat Biotechnol, 34*(2), 184-191. doi:10.1038/nbt.3437

Erlendsson, S., Morado, D. R., Cullen, H. B., Feschotte, C., Shepherd, J. D., & Briggs, J. A. G. (2020). Structures of virus-like capsids formed by the Drosophila neuronal Arc proteins. *Nat Neurosci, 23*(2), 172-175. doi:10.1038/s41593-019-0569-y

Garcia-Martin, R., Wang, G., Brandao, B. B., Zanotto, T. M., Shah, S., Kumar Patel, S., . . . Kahn, C. R. (2022). MicroRNA sequence codes for small extracellular vesicle release and cellular retention. *Nature, 601*(7893), 446-451. doi:10.1038/s41586-021-04234-3

933 Grosshans, H., Lecointe, F., Grosjean, H., Hurt, E., & Simos, G. (2001). Pus1p-dependent tRNA
934 pseudouridinylation becomes essential when tRNA biogenesis is compromised in yeast.
935 *J Biol Chem, 276*(49), 46333-46339. doi:10.1074/jbc.M107141200

936 Gustafsson, H. T., Ferguson, L., Galan, C., Yu, T., Upton, H., Kaymak, E., . . . Rando, O. J. (2025).
937 Deep sequencing of yeast and mouse tRNAs and tRNA fragments using OTTR. *Elife, 14*.
938 doi:10.7554/eLife.77616

939 Henriques, W. S., Young, J. M., Nemudryi, A., Nemudraia, A., Wiedenheft, B., & Malik, H. S.
940 (2024). The Diverse Evolutionary Histories of Domesticated Metaviral Capsid Genes in
941 Mammals. *Mol Biol Evol, 41*(4). doi:10.1093/molbev/msae061

942 Herridge, R. P., Dolata, J., Migliori, V., de Santis Alves, C., Borges, F., Schorn, A. J., . . .
943 Martienssen, R. A. (2025). Pseudouridine guides germline small RNA transport and
944 epigenetic inheritance. *Nat Struct Mol Biol, 32*(2), 277-286. doi:10.1038/s41594-024-
945 01392-6

946 Holliday, L. S., Faria, L. P., & Rody, W. J., Jr. (2019). Actin and Actin-Associated Proteins in
947 Extracellular Vesicles Shed by Osteoclasts. *Int J Mol Sci, 21*(1).
948 doi:10.3390/ijms21010158

949 Huang, D. W., Sherman, B. T., & Lempicki, R. A. (2008). Systematic and integrative analysis of
950 large gene lists using DAVID bioinformatics resources. *Nature Protocols, 4*(1), 44-57.
951 doi:10.1038/nprot.2008.211

952 Huo, L., Du, X., Li, X., Liu, S., & Xu, Y. (2021). The Emerging Role of Neural Cell-Derived
953 Exosomes in Intercellular Communication in Health and Neurodegenerative Diseases.
954 *Front Neurosci, 15*, 738442. doi:10.3389/fnins.2021.738442

955 Kaletsky, R., Moore, R. S., Vrla, G. D., Parsons, L. R., Gitai, Z., & Murphy, C. T. (2020). C. elegans
956 interprets bacterial non-coding RNAs to learn pathogenic avoidance. *Nature, 586*(7829),
957 445-451. doi:10.1038/s41586-020-2699-5

958 Kammers, K., Cole, R. N., Tiengwe, C., & Ruczinski, I. (2015). Detecting Significant Changes in
959 Protein Abundance. *EuPA Open Proteom, 7*, 11-19. doi:10.1016/j.euprot.2015.02.002

960 Kampmann, M. (2018). CRISPRi and CRISPRa Screens in Mammalian Cells for Precision
961 Biology and Medicine. *ACS Chem Biol, 13*(2), 406-416. doi:10.1021/acschembio.7b00657

962 Korkut, C., Ataman, B., Ramachandran, P., Ashley, J., Barria, R., Gherbesi, N., & Budnik, V.
963 (2009). Trans-synaptic transmission of vesicular Wnt signals through Evi/Wntless. *Cell,*
964 *139*(2), 393-404. doi:10.1016/j.cell.2009.07.051

965 Kugeratski, F. G., Hodge, K., Lilla, S., McAndrews, K. M., Zhou, X., Hwang, R. F., . . . Kalluri, R.
966 (2021). Quantitative proteomics identifies the core proteome of exosomes with syntenin-
967 1 as the highest abundant protein and a putative universal biomarker. *Nat Cell Biol, 23*(6),
968 631-641. doi:10.1038/s41556-021-00693-y

969 Kuncha, S. K., Mazeed, M., Singh, R., Kattula, B., Routh, S. B., & Sankaranarayanan, R. (2018).
970 A chiral selectivity relaxed paralog of DTD for proofreading tRNA mischarging in Animalia.
971 *Nat Commun, 9*(1), 511. doi:10.1038/s41467-017-02204-w

Kunitake, K., Mizuno, T., Hattori, K., Oneyama, C., Kamiya, M., Ota, S., . . . Kojima, R. (2024). Barcoding of small extracellular vesicles with CRISPR-gRNA enables comprehensive, subpopulation-specific analysis of their biogenesis and release regulators. *Nat Commun, 15*(1), 9777. doi:10.1038/s41467-024-53736-x

Langmead, B., & Salzberg, S. L. (2012). Fast gapped-read alignment with Bowtie 2. *Nat Methods, 9*(4), 357-359. doi:10.1038/nmeth.1923

Lawrence, M., Huber, W., Pages, H., Aboyoun, P., Carlson, M., Gentleman, R., . . . Carey, V. J. (2013). Software for computing and annotating genomic ranges. *PLoS Comput Biol, 9*(8), e1003118. doi:10.1371/journal.pcbi.1003118

Leidal, A. M., Huang, H. H., Marsh, T., Solvik, T., Zhang, D., Ye, J., . . . Debnath, J. (2020). The LC3-conjugation machinery specifies the loading of RNA-binding proteins into extracellular vesicles. *Nat Cell Biol, 22*(2), 187-199. doi:10.1038/s41556-019-0450-y

Li, J. B., & Walkley, C. R. (2025). Leveraging genetics to understand ADAR1-mediated RNA editing in health and disease. *Nat Rev Genet, 26*(8), 532-546. doi:10.1038/s41576-025-00830-5

Li, W., Xu, H., Xiao, T., Cong, L., Love, M. I., Zhang, F., . . . Liu, X. S. (2014). MAGeCK enables robust identification of essential genes from genome-scale CRISPR/Cas9 knockout screens. *Genome Biol, 15*(12), 554. doi:10.1186/s13059-014-0554-4

Liu, X. M., Ma, L., & Schekman, R. (2021). Selective sorting of microRNAs into exosomes by phase-separated YBX1 condensates. *Elife, 10*. doi:10.7554/eLife.71982

Love, M. I., Huber, W., & Anders, S. (2014). Moderated estimation of fold change and dispersion for RNA-seq data with DESeq2. *Genome Biol, 15*(12), 550. doi:10.1186/s13059-014-0550-8

Lu, A., Wawro, P., Morgens, D. W., Portela, F., Bassik, M. C., & Pfeffer, S. R. (2018). Genome-wide interrogation of extracellular vesicle biology using barcoded miRNAs. *Elife, 7*. doi:10.7554/eLife.41460

M'Angale, P. G., Lemieux, A., Liu, Y., Wang, S., Zinter, M., Alegre, G., . . . Thomson, T. (2025). Capsid transfer of the retrotransposon Copia controls structural synaptic plasticity in Drosophila. *PLoS Biol, 23*(2), e3002983. doi:10.1371/journal.pbio.3002983

Ma, L., Lu, H., Tian, Z., Yang, M., Ma, J., Shang, G., . . . Chen, Z. (2022). Structural insights into the interactions and epigenetic functions of human nucleic acid repair protein ALKBH6. *J Biol Chem, 298*(3), 101671. doi:10.1016/j.jbc.2022.101671

Madigan, V., Zhang, Y., Raghavan, R., Wilkinson, M. E., Faure, G., Puccio, E., . . . Zhang, F. (2024). Human paraneoplastic antigen Ma2 (PNMA2) forms icosahedral capsids that can be engineered for mRNA delivery. *Proc Natl Acad Sci U S A, 121*(11), e2307812120. doi:10.1073/pnas.2307812120

Maori, E., Garbian, Y., Kunik, V., Mozes-Koch, R., Malka, O., Kalev, H., . . . Shafir, S. (2019). A Transmissible RNA Pathway in Honey Bees. *Cell Rep, 27*(7), 1949-1959 e1946. doi:10.1016/j.celrep.2019.04.073

1011 Marangon, D., Castro, E. S. J. H., & Lecca, D. (2022). Neuronal and Glial Communication via
1012 Non-Coding RNAs: Messages in Extracellular Vesicles. *Int J Mol Sci, 24*(1).
1013 doi:10.3390/ijms24010470

1014 Martin, M. (2011). Cutadapt removes adapter sequences from high-throughput sequencing reads.
1015 *EMBnet.journal, 17*(1). doi:10.14806/ej.17.1.200

1016 Matsui, T., Osaki, F., Hiragi, S., Sakamaki, Y., & Fukuda, M. (2021). ALIX and ceramide
1017 differentially control polarized small extracellular vesicle release from epithelial cells.
1018 *EMBO Rep, 22*(5), e51475. doi:10.15252/embr.202051475

1019 Mews, P., Donahue, G., Drake, A. M., Luczak, V., Abel, T., & Berger, S. L. (2017). Acetyl-CoA
1020 synthetase regulates histone acetylation and hippocampal memory. *Nature, 546*(7658),
1021 381-386. doi:10.1038/nature22405

1022 Mittelbrunn, M., Gutierrez-Vazquez, C., Villarroya-Beltri, C., Gonzalez, S., Sanchez-Cabo, F.,
1023 Gonzalez, M. A., . . . Sanchez-Madrid, F. (2011). Unidirectional transfer of microRNA-
1024 loaded exosomes from T cells to antigen-presenting cells. *Nat Commun, 2*, 282.
1025 doi:10.1038/ncomms1285

1026 Moller, A., & Lobb, R. J. (2020). The evolving translational potential of small extracellular vesicles
1027 in cancer. *Nat Rev Cancer, 20*(12), 697-709. doi:10.1038/s41568-020-00299-w

1028 Molnar, A., Melnyk, C. W., Bassett, A., Hardcastle, T. J., Dunn, R., & Baulcombe, D. C. (2010).
1029 Small silencing RNAs in plants are mobile and direct epigenetic modification in recipient
1030 cells. *Science, 328*(5980), 872-875. doi:10.1126/science.1187959

1031 Moore, R. S., Kaletsky, R., Lesnik, C., Cota, V., Blackman, E., Parsons, L. R., . . . Murphy, C. T.
1032 (2021). The role of the Cer1 transposon in horizontal transfer of transgenerational
1033 memory. *Cell, 184*(18), 4697-4712 e4618. doi:10.1016/j.cell.2021.07.022

1034 Murillo, O. D., Thistlethwaite, W., Rozowsky, J., Subramanian, S. L., Lucero, R., Shah, N., . . .
1035 Milosavljevic, A. (2019). exRNA Atlas Analysis Reveals Distinct Extracellular RNA Cargo
1036 Types and Their Carriers Present across Human Biofluids. *Cell, 177*(2), 463-477 e415.
1037 doi:10.1016/j.cell.2019.02.018

1038 Nechooshtan, G., Yunusov, D., Chang, K., & Gingeras, T. R. (2020). Processing by RNase 1
1039 forms tRNA halves and distinct Y RNA fragments in the extracellular environment. *Nucleic*
1040 *Acids Res, 48*(14), 8035-8049. doi:10.1093/nar/gkaa526

1041 O'Brien, K., Breyne, K., Ughetto, S., Laurent, L. C., & Breakefield, X. O. (2020). RNA delivery by
1042 extracellular vesicles in mammalian cells and its applications. *Nat Rev Mol Cell Biol,*
1043 *21*(10), 585-606. doi:10.1038/s41580-020-0251-y

1044 Pastuzyn, E. D., Day, C. E., Kearns, R. B., Kyrke-Smith, M., Taibi, A. V., McCormick, J., . . .
1045 Shepherd, J. D. (2018). The Neuronal Gene Arc Encodes a Repurposed Retrotransposon
1046 Gag Protein that Mediates Intercellular RNA Transfer. *Cell, 172*(1-2), 275-288 e218.
1047 doi:10.1016/j.cell.2017.12.024

1048 Patton, J. R., Bykhovskaya, Y., Mengesha, E., Bertolotto, C., & Fischel-Ghodsian, N. (2005).
1049 Mitochondrial myopathy and sideroblastic anemia (MLASA): missense mutation in the

1050 pseudouridine synthase 1 (PUS1) gene is associated with the loss of tRNA
1051 pseudouridylation. *J Biol Chem, 280*(20), 19823-19828. doi:10.1074/jbc.M500216200

1052 Qi, Y., Wang, J. K., McMillian, M., & Chikaraishi, D. M. (1997). Characterization of a CNS cell line,
1053 CAD, in which morphological differentiation is initiated by serum deprivation. *J Neurosci,*
1054 *17*(4), 1217-1225. doi:10.1523/JNEUROSCI.17-04-01217.1997

1055 Qu, S., Nelson, H. M., Liu, X., Wang, Y., Semler, E. M., Michell, D. L., . . . Patton, J. G. (2024). 5-
1056 Fluorouracil treatment represses pseudouridine-containing miRNA export into
1057 extracellular vesicles. *J Extracell Biol, 3*(9), e70010. doi:10.1002/jex2.70010

1058 Quinlan, A. R. (2014). BEDTools: The Swiss-Army Tool for Genome Feature Analysis. *Curr*
1059 *Protoc Bioinformatics, 47*, 11 12 11-34. doi:10.1002/0471250953.bi1112s47

1060 Reggiori, F., Wang, C. W., Stromhaug, P. E., Shintani, T., & Klionsky, D. J. (2003). Vps51 is part
1061 of the yeast Vps fifty-three tethering complex essential for retrograde traffic from the early
1062 endosome and Cvt vesicle completion. *J Biol Chem, 278*(7), 5009-5020.
1063 doi:10.1074/jbc.M210436200

1064 Rintala-Dempsey, A. C., & Kothe, U. (2017). Eukaryotic stand-alone pseudouridine synthases -
1065 RNA modifying enzymes and emerging regulators of gene expression? *RNA Biol, 14*(9),
1066 1185-1196. doi:10.1080/15476286.2016.1276150

1067 Ritchie, M. E., Phipson, B., Wu, D., Hu, Y., Law, C. W., Shi, W., & Smyth, G. K. (2015). limma
1068 powers differential expression analyses for RNA-sequencing and microarray studies.
1069 *Nucleic Acids Res, 43*(7), e47. doi:10.1093/nar/gkv007

1070 Rorbach, J., Boesch, P., Gammage, P. A., Nicholls, T. J., Pearce, S. F., Patel, D., . . . Minczuk,
1071 M. (2014). MRM2 and MRM3 are involved in biogenesis of the large subunit of the
1072 mitochondrial ribosome. *Mol Biol Cell, 25*(17), 2542-2555. doi:10.1091/mbc.E14-01-0014

1073 Ruan, L. L., Zhou, X. L., Tan, M., & Wang, E. D. (2013). Human cytoplasmic ProX edits
1074 mischarged tRNAPro with amino acid but not tRNA specificity. *Biochem J, 450*(1), 243-
1075 252. doi:10.1042/BJ20121493

1076 Rubio Gomez, M. A., & Ibba, M. (2020). Aminoacyl-tRNA synthetases. *RNA, 26*(8), 910-936.
1077 doi:10.1261/rna.071720.119

1078 Sanson, K. R., Hanna, R. E., Hegde, M., Donovan, K. F., Strand, C., Sullender, M. E., . . . Doench,
1079 J. G. (2018). Optimized libraries for CRISPR-Cas9 genetic screens with multiple
1080 modalities. *Nat Commun, 9*(1), 5416. doi:10.1038/s41467-018-07901-8

1081 Santangelo, L., Giurato, G., Cicchini, C., Montaldo, C., Mancone, C., Tarallo, R., . . . Tripodi, M.
1082 (2016). The RNA-Binding Protein SYNCRIP Is a Component of the Hepatocyte Exosomal
1083 Machinery Controlling MicroRNA Sorting. *Cell Rep, 17*(3), 799-808.
1084 doi:10.1016/j.celrep.2016.09.031

1085 Scacchetti, A., Shields, E. J., Trigg, N. A., Lee, G. S., Wilusz, J. E., Conine, C. C., & Bonasio, R.
1086 (2024). A ligation-independent sequencing method reveals tRNA-derived RNAs with
1087 blocked 3' termini. *Mol Cell, 84*(19), 3843-3859 e3848. doi:10.1016/j.molcel.2024.07.008

Schwartz, S., Bernstein, D. A., Mumbach, M. R., Jovanovic, M., Herbst, R. H., Leon-Ricardo, B. X., . . . Regev, A. (2014). Transcriptome-wide mapping reveals widespread dynamic-regulated pseudouridylation of ncRNA and mRNA. *Cell, 159*(1), 148-162. doi:10.1016/j.cell.2014.08.028

Segel, M., Lash, B., Song, J., Ladha, A., Liu, C. C., Jin, X., . . . Zhang, F. (2021). Mammalian retrovirus-like protein PEG10 packages its own mRNA and can be pseudotyped for mRNA delivery. *Science, 373*(6557), 882-889. doi:10.1126/science.abg6155

Shalem, O., Sanjana, N. E., Hartenian, E., Shi, X., Scott, D. A., Mikkelson, T., . . . Zhang, F. (2014). Genome-scale CRISPR-Cas9 knockout screening in human cells. *Science, 343*(6166), 84-87. doi:10.1126/science.1247005

Sharma, S., Jiao, X., Yang, J., Kwan, K. Y., & Kiledjian, M. (2025). Extracellular exosomal RNAs are glyco-modified. *Nature Cell Biology, 27*(6), 983-991. doi:10.1038/s41556-025-01682-1

Sherman, B. T., Hao, M., Qiu, J., Jiao, X., Baseler, M. W., Lane, H. C., . . . Chang, W. (2022). DAVID: a web server for functional enrichment analysis and functional annotation of gene lists (2021 update). *Nucleic Acids Res, 50*(W1), W216-W221. doi:10.1093/nar/gkac194

Shurtleff, M. J., Temoche-Diaz, M. M., Karfilis, K. V., Ri, S., & Schekman, R. (2016). Y-box protein 1 is required to sort microRNAs into exosomes in cells and in a cell-free reaction. *Elife, 5*. doi:10.7554/eLife.19276

Shurtleff, M. J., Yao, J., Qin, Y., Nottingham, R. M., Temoche-Diaz, M. M., Schekman, R., & Lambowitz, A. M. (2017). Broad role for YBX1 in defining the small noncoding RNA composition of exosomes. *Proc Natl Acad Sci U S A, 114*(43), E8987-E8995. doi:10.1073/pnas.1712108114

Smith, T., Heger, A., & Sudbery, I. (2017). UMI-tools: modeling sequencing errors in Unique Molecular Identifiers to improve quantification accuracy. *Genome Res, 27*(3), 491-499. doi:10.1101/gr.209601.116

Sonder, S. L., Boye, T. L., Tolle, R., Dengjel, J., Maeda, K., Jaattela, M., . . . Nylandsted, J. (2019). Annexin A7 is required for ESCRT III-mediated plasma membrane repair. *Sci Rep, 9*(1), 6726. doi:10.1038/s41598-019-43143-4

Sullivan, K. R., Ravens, A., Walker, A. C., & Shepherd, J. D. (2025). "Arc - A viral vector of memory and synaptic plasticity". *Curr Opin Neurobiol, 91*, 102979. doi:10.1016/j.conb.2025.102979

Sun, C., Guo, R., Ye, X., Tang, S., Chen, M., Zhou, P., . . . Hu, H. (2024). Wybutosine hypomodification of tRNAphe activates HERVK and impairs neuronal differentiation. *iScience, 27*(5), 109748. doi:10.1016/j.isci.2024.109748

Takakura, M., Ishiguro, K., Akichika, S., Miyauchi, K., & Suzuki, T. (2019). Biogenesis and functions of aminocarboxypropyluridine in tRNA. *Nat Commun, 10*(1), 5542. doi:10.1038/s41467-019-13525-3

1126 Tartaglia, G. G., Hollas, H., Havik, B., Vedeler, A., & Pastore, A. (2025). The RNA-Binding
1127 Properties of Annexins. *J Mol Biol, 437*(4), 168933. doi:10.1016/j.jmb.2024.168933

1128 Tassetto, M., Kunitomi, M., & Andino, R. (2017). Circulating Immune Cells Mediate a Systemic
1129 RNAi-Based Adaptive Antiviral Response in Drosophila. *Cell, 169*(2), 314-325 e313.
1130 doi:10.1016/j.cell.2017.03.033

1131 Thery, C., Amigorena, S., Raposo, G., & Clayton, A. (2006). Isolation and characterization of
1132 exosomes from cell culture supernatants and biological fluids. *Curr Protoc Cell Biol,*
1133 *Chapter 3*, Unit 3 22. doi:10.1002/0471143030.cb0322s30

1134 Toribio, V., & Yanez-Mo, M. (2022). Tetraspanins interweave EV secretion, endosomal network
1135 dynamics and cellular metabolism. *Eur J Cell Biol, 101*(3), 151229.
1136 doi:10.1016/j.ejcb.2022.151229

1137 Tosar, J. P., & Cayota, A. (2020). Extracellular tRNAs and tRNA-derived fragments. *RNA Biol,*
1138 *17*(8), 1149-1167. doi:10.1080/15476286.2020.1729584

1139 Tosar, J. P., Segovia, M., Castellano, M., Gambaro, F., Akiyama, Y., Fagundez, P., . . . Cayota,
1140 A. (2020). Fragmentation of extracellular ribosomes and tRNAs shapes the extracellular
1141 RNAome. *Nucleic Acids Res, 48*(22), 12874-12888. doi:10.1093/nar/gkaa674

1142 Tosar, J. P., Witwer, K., & Cayota, A. (2021). Revisiting Extracellular RNA Release, Processing,
1143 and Function. *Trends Biochem Sci, 46*(6), 438-445. doi:10.1016/j.tibs.2020.12.008

1144 Trigg, N. A., & Conine, C. C. (2024). Epididymal acquired sperm microRNAs modify post-
1145 fertilization embryonic gene expression. *Cell Rep, 43*(9), 114698.
1146 doi:10.1016/j.celrep.2024.114698

1147 Upton, H. E., Ferguson, L., Temoche-Diaz, M. M., Liu, X. M., Pimentel, S. C., Ingolia, N. T., . . .
1148 Collins, K. (2021). Low-bias ncRNA libraries using ordered two-template relay: Serial
1149 template jumping by a modified retroelement reverse transcriptase. *Proc Natl Acad Sci U*
1150 *S A, 118*(42). doi:10.1073/pnas.2107900118

1151 Valadi, H., Ekstrom, K., Bossios, A., Sjostrand, M., Lee, J. J., & Lotvall, J. O. (2007). Exosome-
1152 mediated transfer of mRNAs and microRNAs is a novel mechanism of genetic exchange
1153 between cells. *Nature cell biology, 9*(6), 654-659. doi:10.1038/ncb1596

1154 van Niel, G., D'Angelo, G., & Raposo, G. (2018). Shedding light on the cell biology of extracellular
1155 vesicles. *Nat Rev Mol Cell Biol, 19*(4), 213-228. doi:10.1038/nrm.2017.125

1156 Villarroya-Beltri, C., Gutierrez-Vazquez, C., Sanchez-Cabo, F., Perez-Hernandez, D., Vazquez,
1157 J., Martin-Cofreces, N., . . . Sanchez-Madrid, F. (2013). Sumoylated hnRNPA2B1 controls
1158 the sorting of miRNAs into exosomes through binding to specific motifs. *Nat Commun, 4*,
1159 2980. doi:10.1038/ncomms3980

1160 Wang, H., & Oxford, G. S. (2000). Voltage-dependent ion channels in CAD cells: A
1161 catecholaminergic neuronal line that exhibits inducible differentiation. *J Neurophysiol,*
1162 *84*(6), 2888-2895. doi:10.1152/jn.2000.84.6.2888

1163 Wang, Z. Y., Wen, Z. J., Xu, H. M., Zhang, Y., & Zhang, Y. F. (2022). Exosomal noncoding RNAs
1164 in central nervous system diseases: biological functions and potential clinical applications.
1165 *Front Mol Neurosci, 15*, 1004221. doi:10.3389/fnmol.2022.1004221

1166 Wei, S., Dai, X., Yuan, J., He, S., Shah, K., Guo, S., . . . Wang, Y. (2025). Quantitative Proteomics
1167 Identifies Profilin-1 as a Pseudouridine-Binding Protein. *J Am Chem Soc, 147*(2), 1458-
1168 1462. doi:10.1021/jacs.4c17659

1169 Welsh, J. A., Goberdhan, D. C. I., O'Driscoll, L., Buzas, E. I., Blenkiron, C., Bussolati, B., . . .
1170 Witwer, K. W. (2024). Minimal information for studies of extracellular vesicles
1171 (MISEV2023): From basic to advanced approaches. *J Extracell Vesicles, 13*(2), e12404.
1172 doi:10.1002/jev2.12404

1173 Xie, Y., Chai, P., Till, N. A., Hemberger, H., Lebedenko, C. G., Porat, J., . . . Flynn, R. A. (2024).
1174 The modified RNA base acp(3)U is an attachment site for N-glycans in glycoRNA. *Cell,*
1175 *187*(19), 5228-5237 e5212. doi:10.1016/j.cell.2024.07.044

1176 Xu, J., Erlendsson, S., Singh, M., Holling, G. A., Regier, M., Ibiricu, I., . . . Shepherd, J. D. (2024).
1177 PNMA2 forms immunogenic non-enveloped virus-like capsids associated with
1178 paraneoplastic neurological syndrome. *Cell, 187*(4), 831-845 e819.
1179 doi:10.1016/j.cell.2024.01.009

1180 You, Y., Zhang, Z., Sultana, N., Ericsson, M., Martens, Y. A., Sun, M., . . . Ikezu, T. (2023).
1181 ATP1A3 as a target for isolating neuron-specific extracellular vesicles from human brain
1182 and biofluids. *Sci Adv, 9*(37), eadi3647. doi:10.1126/sciadv.adi3647

1183 Zhang, Y., Parmigiani, G., & Johnson, W. E. (2020). ComBat-seq: batch effect adjustment for
1184 RNA-seq count data. *NAR Genom Bioinform, 2*(3), lqaa078. doi:10.1093/nargab/lqaa078

1185 Zhao, X., Ma, D., Ishiguro, K., Saito, H., Akichika, S., Matsuzawa, I., . . . Suzuki, T. (2023).
1186 Glycosylated queuosines in tRNAs optimize translational rate and post-embryonic growth.
1187 *Cell, 186*(25), 5517-5535 e5524. doi:10.1016/j.cell.2023.10.026

1188 **FIGURE LEGENDS**

1189 **Figure 1. CADs produce EVs enriched in tRNAs and snoRNAs**

1190 (A) Scheme of EV purification protocol. Conditioned medium was collected and subjected to
1191 several round of centrifugation at increasing speeds to remove cells, cell debris, and large
1192 vesicles. In the last step EVs were pelleted via ultracentrifugation at 100,000 x *g*.

1193 (B) Nanoparticle tracking analysis of EVs from CADs. The plot shows the average (n = 2) number
1194 of particles per mL on the *y* axis and their size on the *x* axis. The vertical dashed line indicates
1195 the median size.

1196 (C) Comparison of cellular and EV proteomes by mass spectrometry. Gray, significantly different
1197 proteins (adjusted $p < 0.1$; n = 2); blue, EV markers; yellow, cellular markers.

1198 (D) Top 9 enriched GO terms ("cellular component" aspect) associated with proteins significantly
1199 enriched in EVs from (C).

1200 (E) Gel electrophoresis (2% agarose-formaldehyde) comparing cellular *vs.* EV RNA. Individual
1201 replicates were loaded in separate lanes.

1202 (F) RNA content of CADs *vs.* EVs, measured by deep sequencing (LIDAR). Red, transcripts
1203 significantly enriched in EVs [exRNAs; adjusted $p < 0.1$ and $\log_2$(EVs/cells) > 0; $n \geq 3$].

1204 (G) Same as (F) with different classes of RNA highlighted by colors, as indicated.

1205 **Figure 2. A genome-wide screen identifies regulators of RNA secretion**

1206 (A) Scheme of the genetic screen. CADs were transduced with a lentiviral library containing
1207 sgRNAs against most protein coding genes. Two (baseline) and 10 (readout) days later, cells and
1208 EVs were harvested to measure sgRNA levels.

1209 (B) Hypothetical gene categories with expected changes in sgRNA abundance over time in cells
1210 and EVs. See text for explanation.

1211 (C) Change in sgRNA abundance (n = 4 sgRNAs per gene), compared to their average
1212 abundance in the corresponding sample (cells or EVs) at day 2. Individual biological replicates
1213 (r1 and r2) are shown.

1214 (D) Observed/predicted ratio of sgRNAs targeting putative positive (left) and negative (right)
1215 regulators of RNA secretion, derived from MaGECK analysis. Significant hits (p value < 0.05) are
1216 in red (n = 2). Candidates mentioned in the text are highlighted in blue.

1217 (E) GO analysis (cellular component) of significant positive regulators from (D).

1218 (F) Predicted (gray) vs. observed (red) sgRNA abundances in EVs (± SEM), normalized to the
1219 average predicted abundance (see methods), for retrovirus-derived proteins identified as
1220 significant ($p < 0.05$) positive regulators from MaGECK analysis. Values for individual sgRNAs
1221 are shown.

1222 (G) Same as (F) but for RNA-modifying enzymes.

1223 **Figure 3. PUS1 facilitates the export of select exRNAs**

1224 (A) Western blot probing for PUS1, SDCBP, and β-TUB (control) in wild type (WT) and 2 different
1225 *Pus1*$^{-/-}$ CAD clones.

1226 (B) Differences in exRNA abundance between wild type and *Pus1*$^{-/-}$, as measured by LIDAR. Red,
1227 transcripts showing significant difference ($n \geq 3$, adjusted p value < 0.1).

1228 (C) Overlap between RNAs less abundant ("DOWN") in *Pus1*$^{-/-}$ cells compared to WT, either inside
1229 the cells (grey, "cellular") or inside EVs (red, "extracellular").

1230 (D) Ratios of RNA abundance in EVs and inside cells comparing wild type (blue) and *Pus1*$^{-/-}$ (gold)
1231 CADs. Average and distributions are shown by the boxes and individual transcripts are shown in
1232 points. RNAs were divided in the indicated classes and the p values were obtained with Student's
1233 t tests. Data from ≥ 3 biological replicates.

1234 (E) Scheme showing the different types of known tRNA-derived RNAs (tDRs).

1235 (F) Changes in full-length tRNAs or tDRs between wild type and *Pus1*$^{-/-}$ in cells (grey) or EVs (red).
1236 P values are from a Wilcoxon rank sum test. Data from ≥ 3 biological replicates.

1237 **Figure 4. PUS1-dependent Ψ selects RNA for secretion**

1238 (A) Scheme of the Ψ sequencing approach. Bisulfite-induced deletions were detected with a
1239 modified LIDAR protocol which utilizes $MnCl_2$ during reverse transcription.

1240 (B) Distribution of Ψ-modified RNAs among different classes in CADs and EVs. Data from 2
1241 biological replicates.

1242 (C) Ψ levels, inferred by the % of reads containing a deletion at the corresponding sites, for cellular
1243 RNAs (gray) and exRNAs (red). P value is from a Wilcoxon rank sum test.

1244 (D) Schematic representation of the mouse epididymis, highlighting the region of tissue and EVs
1245 used for our analysis (cauda). The direction of sperm movement is indicated by the arrow.

1246 (E) Same as (C) but for cauda tissue and corresponding EVs

1247 (F) Levels of Ψ modification (% of total reads) at individual exRNA sites in wild type (x axis) vs
1248 *Pus1*$^{-/-}$ (y axis) CAD EVs. PUS1-sensitive sites, where Ψ was reduced in *Pus1*$^{-/-}$ EVs by at least
1249 25%, are in gold. Other Ψ sites are in gray. Data from 2 biological replicates.

1250 (G) Ratio of the abundance of Ψ-containing RNAs in *Pus1*$^{-/-}$ CAD vs. WT cells (left) or EVs (right).
1251 The RNAs were classified as PUS1-independent (gray, "others") and PUS1-sensitive (gold). Only
1252 RNAs with at least one Ψ site detected in the EV fraction were considered. P values are from
1253 Wilcoxon rank sum tests.

1254 (H) % of molecules containing Ψ at the indicated bases according to bisulfite-LIDAR for four
1255 example tRNAs in EVs from wild type (WT) and *Pus1*$^{-/-}$ CAD.

1256 (I) Abundance (log_2-converted, DEseq2 normalized counts) for the full-length tRNAs in (H) in wild
1257 type (gray) or *Pus1*$^{-/-}$ (red) EVs. Asterisks indicate *p* value < 0.05 (calculated by DEseq2).

1258 (J–K) Same as (H) and (I) but for the two indicated snoRNAs.

1259 **Figure 5. Ψ promotes exRNA export through MYL6**

1260 (A) Scheme of the sufficiency experiments shown in (B) and (C). CADs were transfected with
1261 RNAs containing only Ψ or U at uridine positions for 6 hours. Their abundance inside and outside
1262 cells was measured 24 hours later by RT-qPCR (B) or sequencing (C).

1263 (B) Abundance of U- (gray) or Ψ-containing (yellow) RNAs 24 hours after transfection inside and
1264 outside CADs 24 hours after transfection, measured by RT-qPCR. *P* values are from Student's *t*
1265 tests.

1266 (C) Export ratio (CPM_{cells} / CPM_{medium}) for U- (gray) or Ψ-containing (yellow) RNAs, 24 hours after
1267 transfection into CADs. Six distinct sequences were tested, indicated by the numbers 1–6. The *p*
1268 values are from Student's *t* tests.

1269 (D) Comparison of protein abundance in the interactome of U- or Ψ-containing RNA, as measured
1270 by mass spectrometry. Dark grey, significantly different proteins (adjusted $p < 0.1$; $n = 2$).

1271 (E) Relative export ratio [export ratio(Ψ) / export ratio(U)] between U- and Ψ-containing RNAs in
1272 the medium from CADs, treated with siRNAs against *Myl6* and control. The different RNA
1273 sequences are identified by the same numbers as in (C). *P* values are from Student's *t* tests.

1274 (F) Differences in exRNA abundance (from conditioned medium) between control and *Myl6*
1275 knockdown (KD) as measured by LIDAR. Red, transcripts showing significant difference ($n \geq 5$,
1276 adjusted *p* value < 0.1).

1277 (G) Ratio of the abundance of RNAs in *Myl6* knock down (KD) vs. control in cells (left) or
1278 conditioned medium (right). The RNAs were classified as U-containing (gray, "others") and Ψ-
1279 containing (blue). Only RNAs with at least one Ψ site detected in EVs were considered. *P* values
1280 are from Wilcoxon rank sum tests.

1281 (H) Proposed model for exRNA secretion. PUS1 marks specific RNAs with Ψ to select them as
1282 exRNAs. Once deposited, Ψ provides a binding site for MYL6, which routes RNAs into EVs
1283 formed via multivesicular bodies or by direct plasma membrane budding.

1284 **SUPPLEMENTAL FIGURE LEGENDS**

1285 **Figure S1. Additional analyses on exRNAs contained in EVs from CADs**

1286 (A) Overlap between the CAD EV proteome (see Fig. 1C) and proteins in the Vesiclepedia
1287 database (Kitti et al., 2024). The *p* value is from a hypergeometric test.

1288 (B) RNA class distribution as % of transcripts significantly (adj. *p* value < 0.1) enriched in cells
1289 compared to EVs and *vice versa*.

1290 (C) Distribution of average ($n \geq 3$) log-fold-changes between cells and EVs for C/D box and H/ACA
1291 box snoRNAs.

1292 (D) Average ($n \geq 3$) insert size distribution of reads mapping to tRNAs in cells and EVs.

1293 (E) Average ($n \geq 3$) tRNA and tDR distribution in cells and EVs.

1294 **Figure S2. Analyses and validations on the genome-wide screen for exRNAs**

1295 (A) RT-qPCR for sgRNA abundance (expressed as ratio to *Rpl32* RNA) in cells and EVs from
1296 sgRNA-expressing CAD and controls.

1297 (B) Scheme of the logic underpinning the genome-wide screen. A fraction of sgRNAs expressed
1298 from a U6 promoter enter endogenous secretion pathways, for example by being loaded into
1299 intraluminal vesicles of multivesicular bodies (MVBs, derived from endosomal maturation) or
1300 directly by budding from the plasma membrane. This allows for the genotype of the originating
1301 cell to be determined via the sgRNA content of the EVs.

1302 (C) Scheme of the LIDAR adaptation used to directly sequence the sgRNAs from the EVs.

1303 (D) Number of sgRNAs that were detected (yellow) or not (blue) in cells and EV in each screen
1304 replicate. Individual samples are shown. Horizontal dashed line indicates the 95% of all sgRNAs
1305 included in the library.

1306 (E) Comparison of the abundance of all individual sgRNAs inside cells vs. EVs at day 2 after
1307 transduction. Red, genes with significant difference ($n = 2$, adjusted *p* value < 0.1)

1308 (F) Nucleotide representation at individual CRISPR RNA (crRNA) targeting sequence positions
1309 for all, preferentially exported, and preferentially retained sgRNAs. The bracket indicates the first
1310 3 positions, enriched for Us in the exported sgRNAs.

1311 (G) Average predicted (gray) and observed (red) values (± SEM) for sgRNAs targeting *Sdcbp.*
1312 Circles represent values for the individual sgRNAs.

1313 (H) Western blot for SDCBP and SUZ12 (control) in wild type and 2 different *Sdcbp*$^{-/-}$ CAD clones.

1314 (I) Nanoparticle tracking analysis of EVs isolated from wild type and *Sdcbp*$^{-/-}$ CADs. The plot
1315 shows the number of particles normalized to the number of starting million cells
1316 [particles/(mL*million cells)] on the y axis and their size on the x axis.

1317 (J) Average particles/(mL*million cells) (± SEM), calculated as in (I), secreted by wild type and 2
1318 different *Sdcbp*$^{-/-}$ CAD clones (n = 3). Individual replicates are shown.

1319 (K) *Z* score-converted mRNA abundance (normalized DEseq2 counts) for the domesticated
1320 retroviral genes showed in Fig. 2F, before ("CAD") and after ("dCAD") CAD cell differentiation into
1321 a more mature neuronal form.

1322 **Figure S3. Validation of *Pus1* and analyses on exRNAs from *Pus1*$^{-/-}$ cells**

1323 (A) Scheme of secondary CRISPRi screen. Stable CADs, transduced with different CRISPRi
1324 sgRNAs were mixed in equal numbers. Then, the abundance of sgRNAs in the pooled cells and
1325 in the tissue culture medium (extracellular) was measured by LIDAR.

1326 (B) Export rate of the indicated CRISPRi sgRNAs, calculated as a ratio of extracellular over
1327 intercellular abundance. "Scr." denotes sgRNA scrambled control. *P* values are from Student's *t*
1328 tests.

1329 (C) Differences in cellular RNA abundance between wild type and *Pus1*$^{-/-}$, as measured by LIDAR.
1330 Red, transcripts showing significant difference ($n \geq 3$, adjusted p value < 0.1).

1331 (D) Overlap between RNAs more abundant ("UP") in *Pus1*$^{-/-}$ cells compared to WT, either inside
1332 the cells (gray, "cellular") or in EVs (red, "extracellular").

1333 (E) Correlations in the change in RNA abundance between wild type and *Pus1*$^{-/-}$ CADs (*x axis*)
1334 and EVs (*y* axis) for the RNAs significantly changed (adjusted p value < 0.1) in either set.
1335 Spearman's correlation values are reported.

1336 **Figure S4. Validation of Ψ sequencing and analyses on exRNAs from *Pus1*$^{-/-}$ CADs**

1337 (A) LIDAR read densities (normalized to counts per millions) for individual nucleotides of an *in*
1338 *vitro*-transcribed Ψ-containing RNA. Top, input; bottom, BID-treated

1339 (B) Inferred % of Ψ based on % of deletion in LIDAR reads mapping to 18s rRNA from CAD RNA.
1340 Top, input; bottom, BID-treated

1341 (C–D) Overlap between Ψ-containing RNAs (C) or individual sites (D) identified in CADs and EVs.
1342 *P* values are from hypergeometric tests.

1343 (E) Denaturing agarose-formaldehyde (2%) electrophoresis of total tissue (cellular) and EV RNA
1344 from cauda epididymis (individual replicates are shown).

1345 (F) Distribution of transcripts containing PUS1-sensitive Ψ sites in CADs and EVs among the
1346 indicated RNA classes. Data from 2 biological replicates.

1347 (G) Distribution of reads containing PUS1-sensitive Ψ sites and mapping to tRNAs genes among
1348 the indicated types of tRNA-derived species in cells and EVs.

1349 (H) % of Ψ modification detected at each canonical tRNA position in wild type or *Pus1*$^{-/-}$ CAD EVs.
1350 Data from the two different *Pus1*$^{-/-}$ clones are shown separately.

1351 (I) % of Ψ at every canonical tRNA position (column) for every tRNA iso-acceptor containing a U
1352 at position 27 (rows) in EVs from wild type (left) or *Pus1*$^{-/-}$ (right) CADs.

1353 (J) Scheme of canonical Ψ sites on tRNAs. In blue, Ψ sites dependent on PUS1.

1354 (K) Overlap between significantly reduced full-length tRNAs in *Pus1*$^{-/-}$ (red) and PUS1 full-length
1355 tRNA targets (yellow) in EVs. *P* value is from a hypergeometric test

1356 (L) Same as (K) but for snoRNAs.

1357 For all panels data were from two biological replicates. In the case of *Pus1*$^{-/-}$ the two individual
1358 knockout clones were used as combined replicates (n = 2 per clone).

1359 **Figure S5. Additional analyses for MYL6**

1360 (A) IP/beads values for U- and Ψ-RNAs interactomes measured by mass spectrometry. In red,
1361 significantly different proteins (adjusted $p < 0.1$; $n = 2$).

1362 (B) MYL6 protein abundance in CADs and EVs.

1363 (C) Average predicted (gray) and observed (red) values (± SEM) for sgRNAs targeting *Myl6.*
1364 Circles represent individual sgRNAs. The *p* value reported is from the MaGECK analysis.

1365 (D) *Myl6* mRNA abundance relative to control (*Rpl32*). Bars show average ± SEM. Individual
1366 replicates are shown.

1367 (E) Differences in intracellular RNA abundance between control and *Myl6* knock down (KD) as
1368 measured by LIDAR. Red, transcripts showing significant difference ($n \geq 5$, adjusted p value <
1369 0.1).

1370 **SUPPLEMENTAL TABLE LEGENDS**

1371 **Table S1. Proteomics of CADs and EVs**

1372 **Table S2. Genome-wide screen results**

1373 **Table S3. RNA-binding proteins within positive regulators of exRNA biogenesis**

1374 **Table S4. Proteomics results from U- and Ψ-containing RNA pulldowns**

1375 **Table S5. Oligonucleotides used in this study**

1376

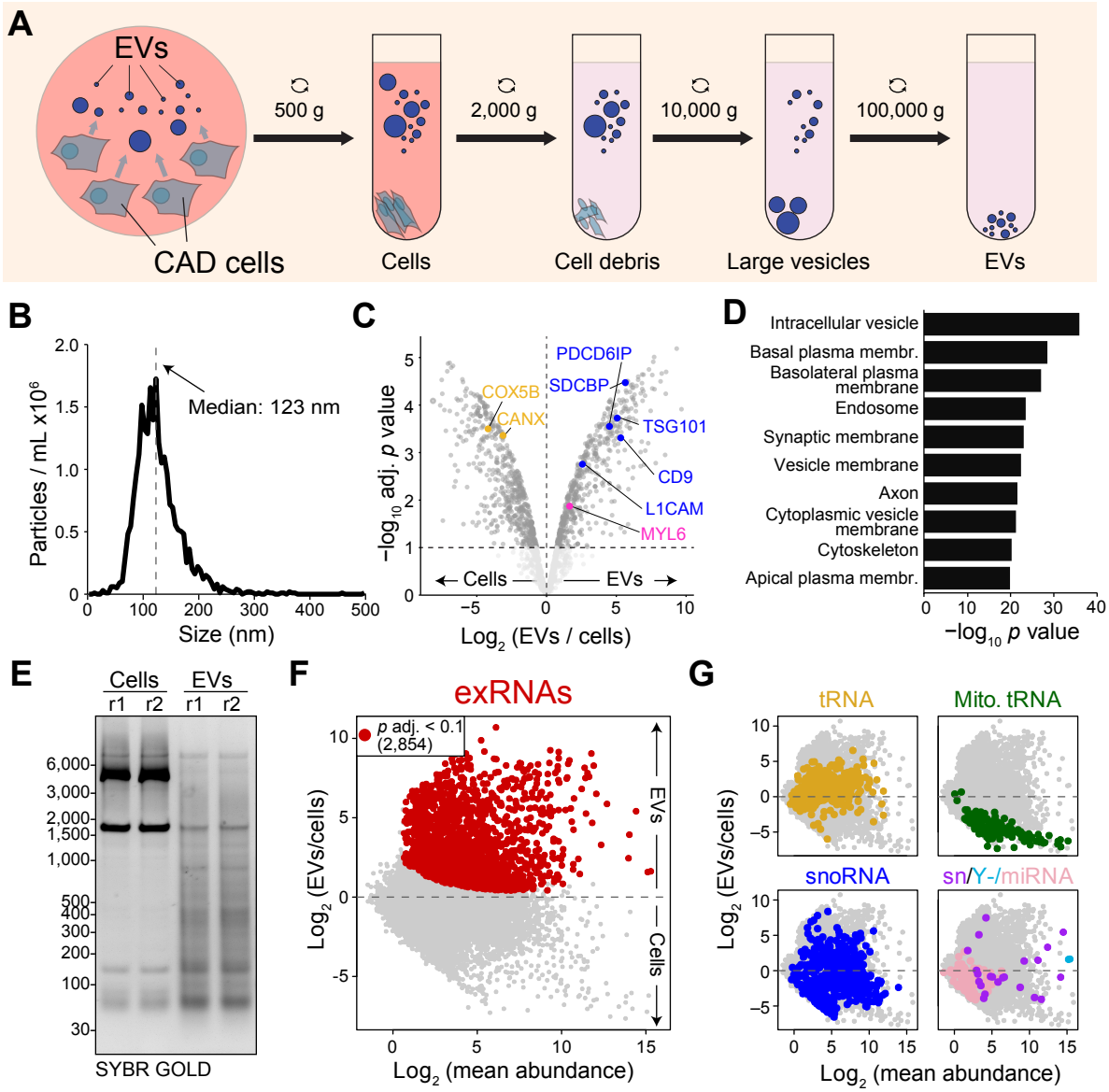

Figure 1. CAD cells produce EVs enriched in tRNAs and snoRNAs

(A) Scheme of EV purification protocol. Conditioned medium was collected and subjected to several round of centrifugation at increasing speeds to remove cells, cell debris, and large vesicles. In the last step EVs were pelleted via ultracentrifugation at 100,000 x g.

(B) Nanoparticle tracking analysis of EVs from CADs. The plot shows the average (n = 2) number of particles per mL on the y axis and their size on the x axis. The vertical dashed line indicates the median size.

(C) Comparison of cellular and EV proteomes by mass spectrometry. Gray, significantly different proteins (adjusted $p < 0.1$; n = 2); blue, EV markers; yellow, cellular markers.

(D) Top 9 enriched GO terms ("cellular component" aspect) associated with proteins significantly enriched in EVs from (C).

(E) Gel electrophoresis (2% agarose-formaldehyde) comparing cellular vs. EV RNA. Individual replicates were loaded in separate lanes.

(F) RNA content of CADs vs. EVs, measured by deep sequencing (LIDAR). Red, transcripts significantly enriched in EVs [exRNAs; adjusted $p < 0.1$ and log2(EVs/cells) > 0; n ≥ 3].

(G) Same as (F) with different classes of RNA highlighted by colors, as indicated.

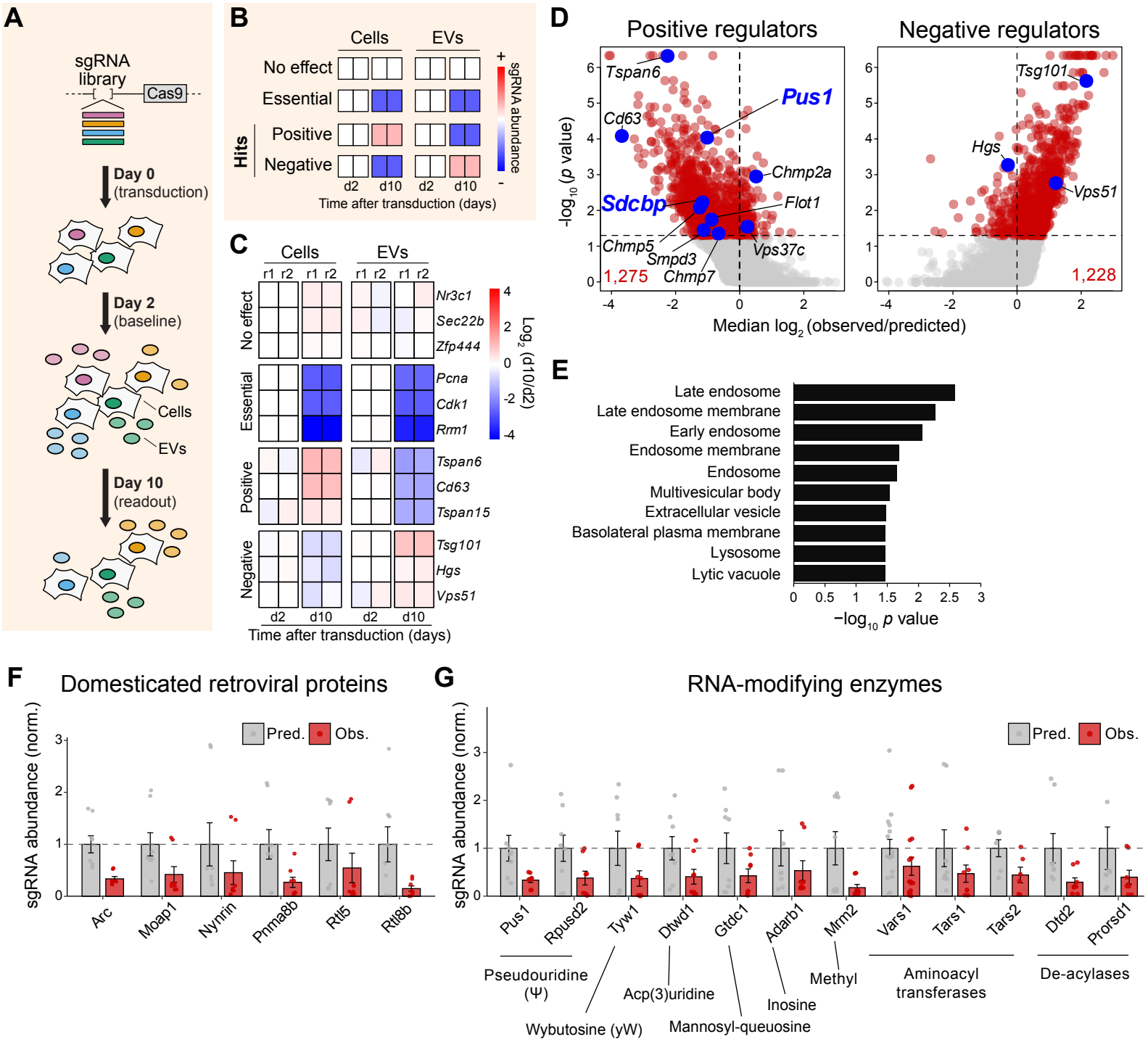

Figure 2. A genome-wide screen identifies regulators of RNA secretion

(A) Scheme of the genetic screen. CADs were transduced with a lentiviral library containing sgRNAs against most protein coding genes. Two (baseline) and 10 (readout) days later, cells and EVs were harvested to measure sgRNA levels.

(B) Hypothetical gene categories with expected changes in sgRNA abundance over time in cells and EVs. See text for explanation.

(C) Change in sgRNA abundance (n = 4 sgRNAs per gene), compared to their average abundance in the corresponding sample (cells or EVs) at day 2. Individual biological replicates (r1 and r2) are shown.

(D) Observed/predicted ratio of sgRNAs targeting putative positive (left) and negative (right) regulators of RNA secretion, derived from MaGECK analysis. Significant hits (p value < 0.05) are in red (n = 2). Candidates mentioned in the text are highlighted in blue.

(E) GO analysis (cellular component) of significant positive regulators from (D).

(F) Predicted (gray) vs. observed (red) sgRNA abundances in EVs (SEM), normalized to the average predicted abundance (see methods), for retrovirus-derived proteins identified as significant (p < 0.05) positive regulators from MaGECK analysis. Values for individual sgRNAs are shown.

(G) Same as (F) but for RNA-modifying enzymes.

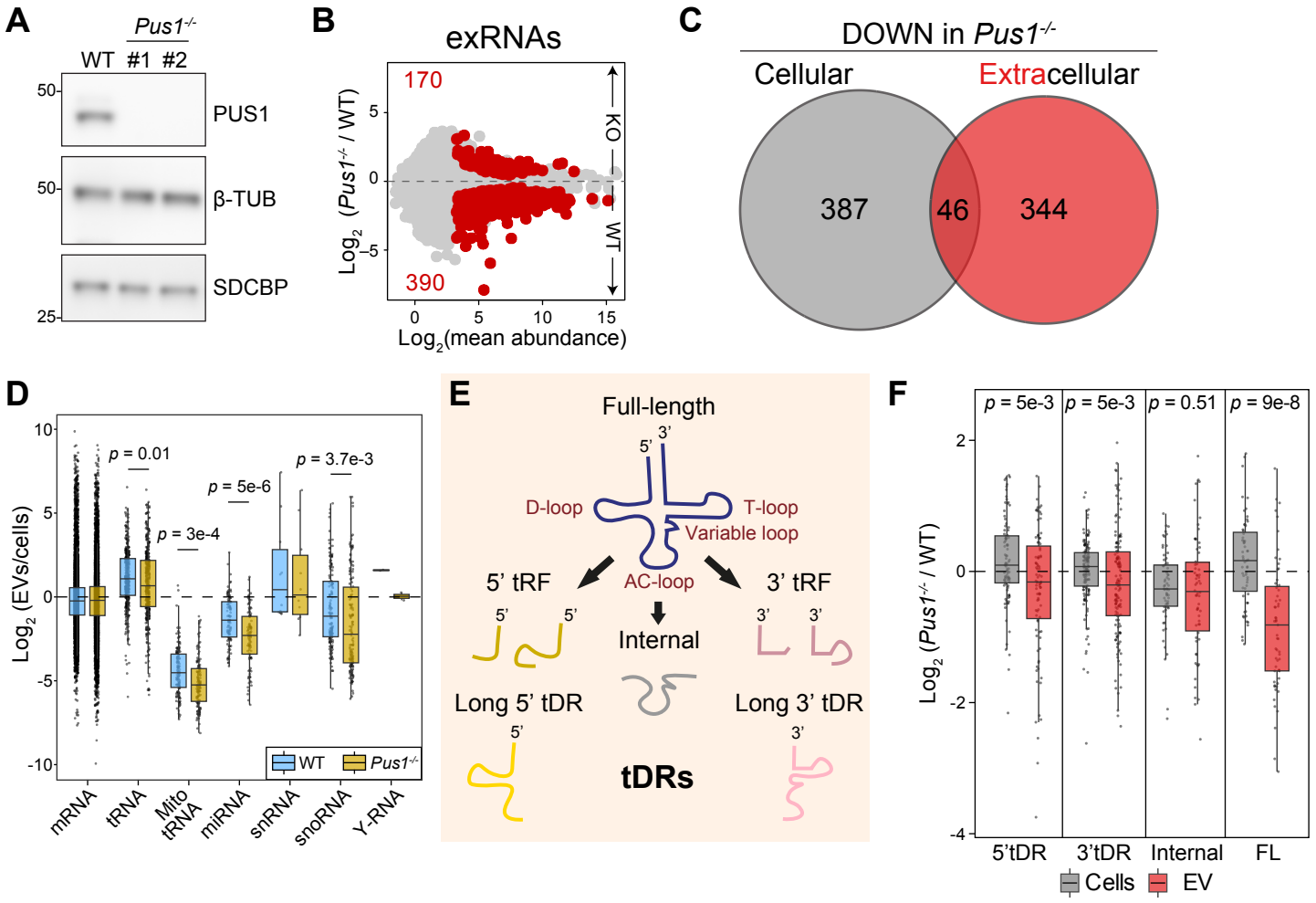

Figure 3. PUS1 facilitates the export of select exRNAs

(A) Western blot probing for PUS1, SDCBP, and β-TUB (control) in wild type (WT) and 2 different Pus1-/- CAD clones.

(B) Differences in exRNA abundance between wild type and Pus1-/-, as measured by LIDAR. Red, transcripts showing significant difference (n ≥ 3, adjusted p value < 0.1).

(C) Overlap between RNAs less abundant ("DOWN") in Pus1-/- cells compared to WT, either inside the cells (grey, "cellular") or inside EVs (red, "extracellular").

(D) Ratios of RNA abundance in EVs and inside cells comparing wild type (blue) and Pus1-/- (gold) CADs. Average and distributions are shown by the boxes and individual transcripts are shown in points. RNAs were divided in the indicated classes and the p values were obtained with Student's t tests. Data from ≥ 3 biological replicates.

(E) Scheme showing the different types of known tRNA-derived RNAs (tDRs).

(F) Changes in full-length tRNAs or tDRs between wild type and Pus1-/- in cells (grey) or EVs (red). P values are from a Wilcoxon rank sum test. Data from ≥ 3 biological replicates

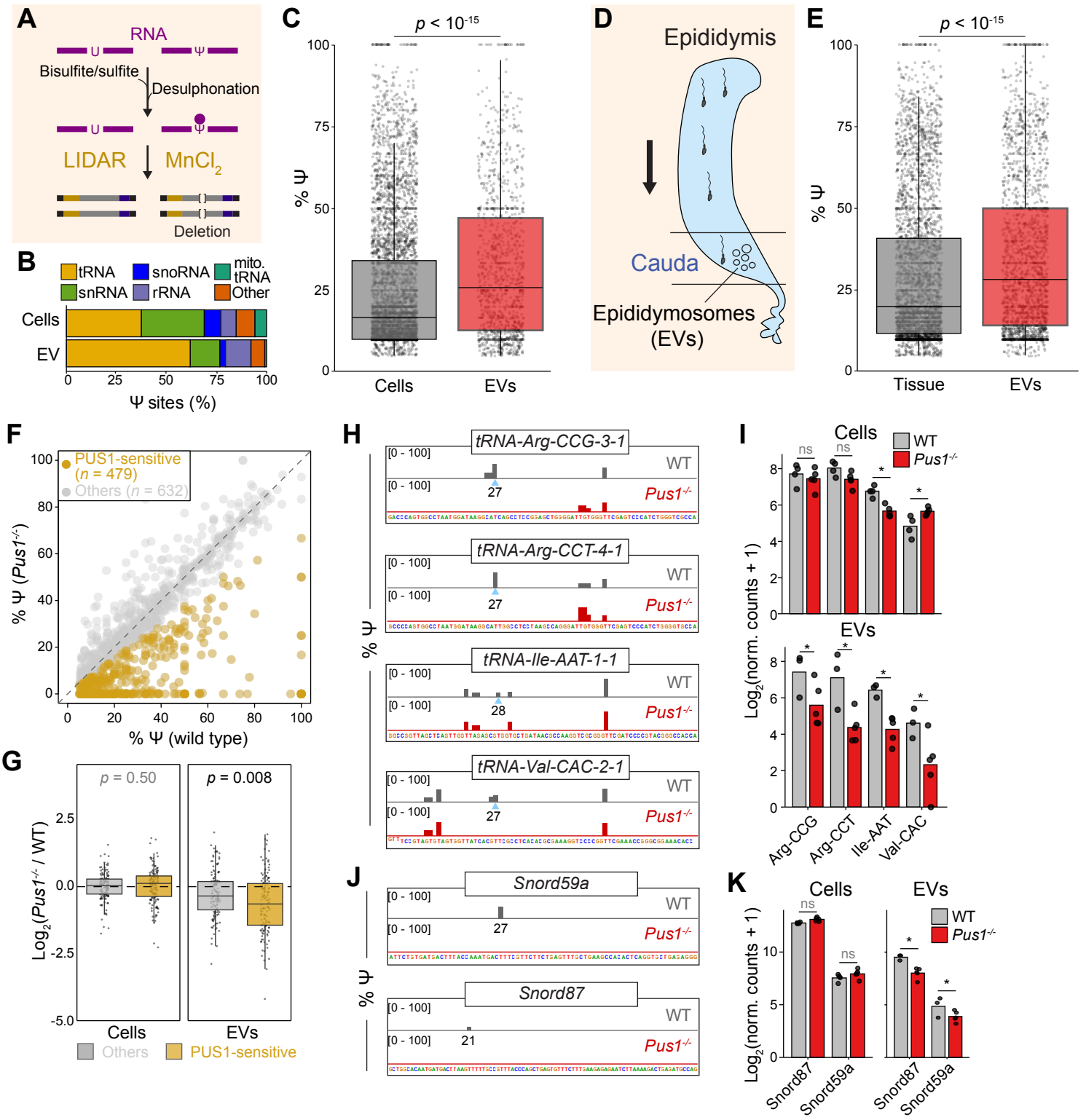

Figure 4. PUS1-dependent Ψ selects RNA for secretion

(A) Scheme of the Ψ sequencing approach. Bisulfite-induced deletions were detected with a modified LIDAR protocol which utilizes MnCl2 during reverse transcription.

(B) Distribution of Ψ-modified RNAs among different classes in CADs and EVs. Data from 2 biological replicates.

(C) Ψ levels, inferred by the % of reads containing a deletion at the corresponding sites, for cellular RNAs (gray) and exRNAs (red). P value is from a Wilcoxon rank sum test.

(D) Schematic representation of the mouse epididymis, highlighting the region of tissue and EVs used for our analysis (cauda). The direction of sperm movement is indicated by the arrow.

(E) Same as (C) but for cauda tissue and corresponding EVs

(F) Levels of Ψ modification (% of total reads) at individual exRNA sites in wild type (x axis) vs Pus1-/- (y axis) CAD EVs. PUS1-sensitive sites, where Ψ was reduced in Pus1-/- EVs by at least 25%, are in gold. Other Ψ sites are in gray. Data from 2 biological replicates.

(G) Ratio of the abundance of Ψ-containing RNAs in Pus1-/- CAD vs. WT cells (left) or EVs (right). The RNAs were classified as PUS1-independent (gray, "others") and PUS1-sensitive (gold). Only RNAs with at least one Ψ site detected in the EV fraction were considered. P values are from Wilcoxon rank sum tests.

(H) % of molecules containing Ψ at the indicated bases according to bisulfite-LIDAR for four example tRNAs in EVs from wild type (WT) and Pus1-/- CAD.

(I) Abundance (log2-converted, DEseq2 normalized counts) for the full-length tRNAs in (H) in wild type (gray) or Pus1-/- (red) EVs. Asterisks indicate p value < 0.05 (calculated by DEseq2).

(J–K) Same as (H) and (I) but for the two indicated snoRNAs.

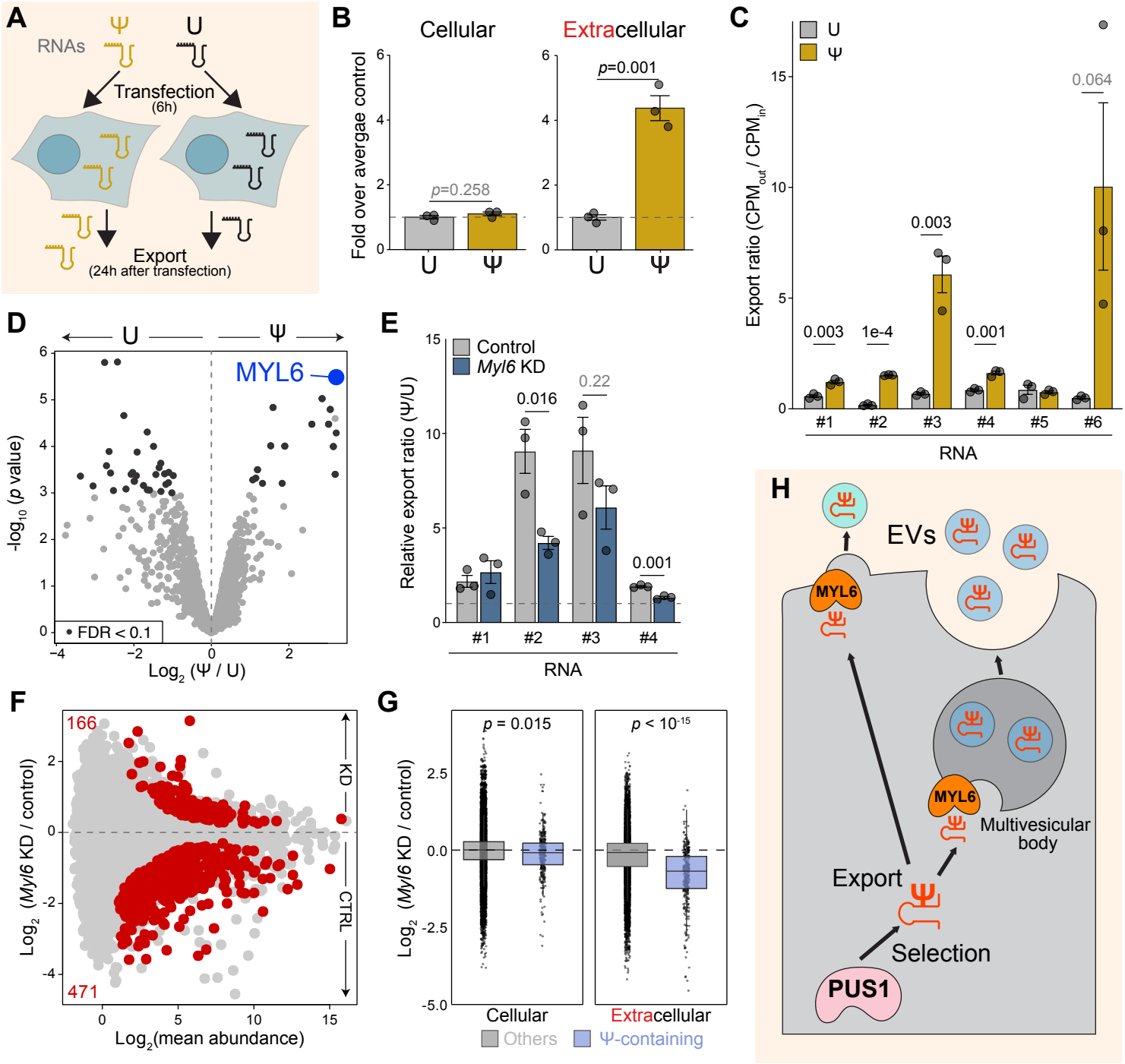

Figure 5. Ψ promotes exRNA export through MYL6

(A) Scheme of the sufficiency experiments shown in (B) and (C). CADs were transfected with RNAs containing only Ψ or U at uridine positions for 6 hours. Their abundance inside and outside cells was measured 24 hours later by RT-qPCR (B) or sequencing (C).

(B) Abundance of U- (gray) or Ψ-containing (yellow) RNAs 24 hours after transfection inside and outside CADs 24 hours after transfection, measured by RT-qPCR. P values are from Student's t tests.

(C) Export ratio (CPMcells / CPMmedium) for U- (gray) or Ψ-containing (yellow) RNAs, 24 hours after transfection into CADs. Six distinct sequences were tested, indicated by the numbers 1–6. The p values are from Student's t tests.

(D) Comparison of protein abundance in the interactome of U- or Ψ-containing RNA, as measured by mass spectrometry. Dark grey, significantly different proteins (adjusted p < 0.1; n = 2).

(E) Relative export ratio [export ratio(Ψ) / export ratio(U)] between U- and Ψ-containing RNAs in the medium from CADs, treated with siRNAs against Myl6 and control. The different RNA sequences are identified by the same numbers as in (C). P values are from Student's t tests.

(F) Differences in exRNA abundance (from conditioned medium) between control and Myl6 knockdown (KD) as measured by LIDAR. Red, transcripts showing significant difference (n ≥ 5, adjusted p value < 0.1).

(G) Ratio of the abundance of RNAs in Myl6 knock down (KD) vs. control in cells (left) or conditioned medium (right). The RNAs were classified as U-containing (gray, "others") and Ψ-containing (blue). Only RNAs with at least one Ψ site detected in EVs were considered. P values are from Wilcoxon rank sum tests.

(H) Proposed model for exRNA secretion. PUS1 marks specific RNAs with Ψ to select them as exRNAs. Once deposited, Ψ provides a binding site for MYL6, which routes RNAs into EVs formed via multivesicular bodies or by direct plasma membrane budding.

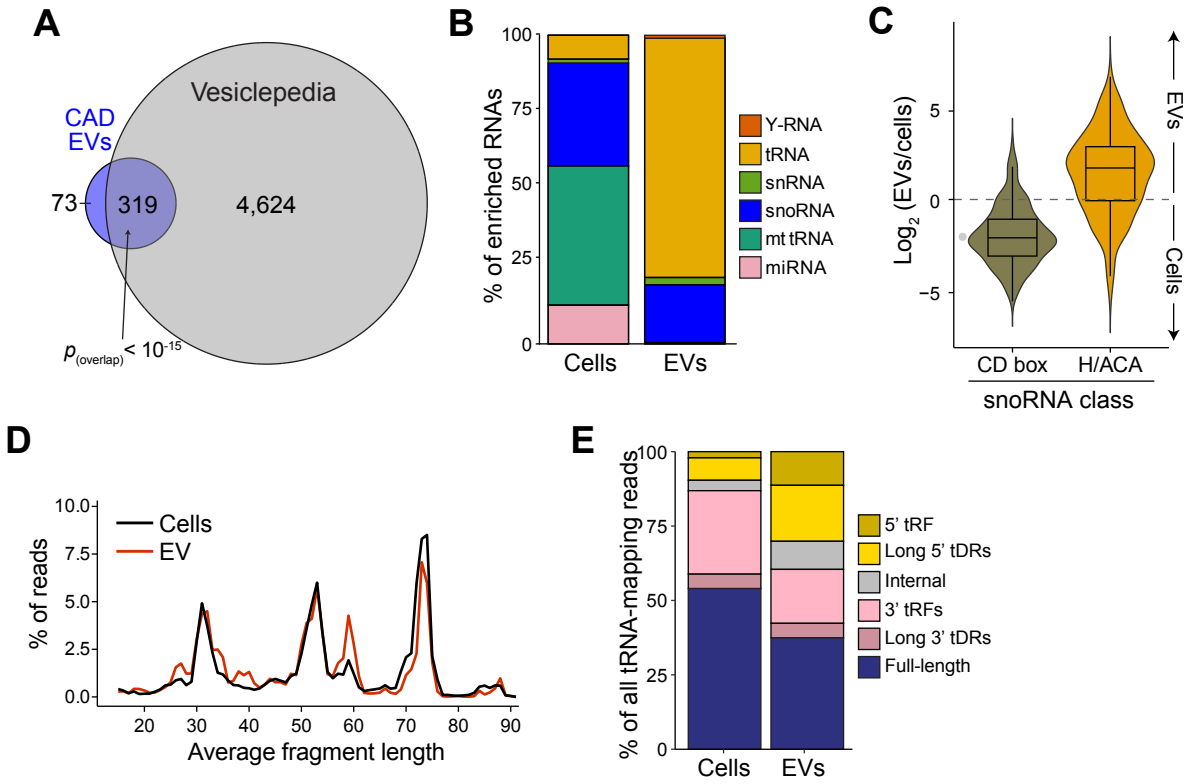

Figure S1. Additional analyses on exRNAs contained in EVs from CAD cells

(A) Overlap between the CAD EV proteome (see Fig. 1C) and proteins in the Vesiclepedia database (Kitti et al., 2024). The p value is from a hypergeometric test.

(B) RNA class distribution as % of transcripts significantly (adj. p value < 0.1) enriched in cells compared to EVs and vice versa.

(C) Distribution of average (n ≥ 3) log-fold-changes between cells and EVs for C/D box and H/ACA box snoRNAs.

(D) Average (n ≥ 3) insert size distribution of reads mapping to tRNAs in cells and EVs.

(E) Average (n ≥ 3) tRNA and tDR distribution in cells and EVs.

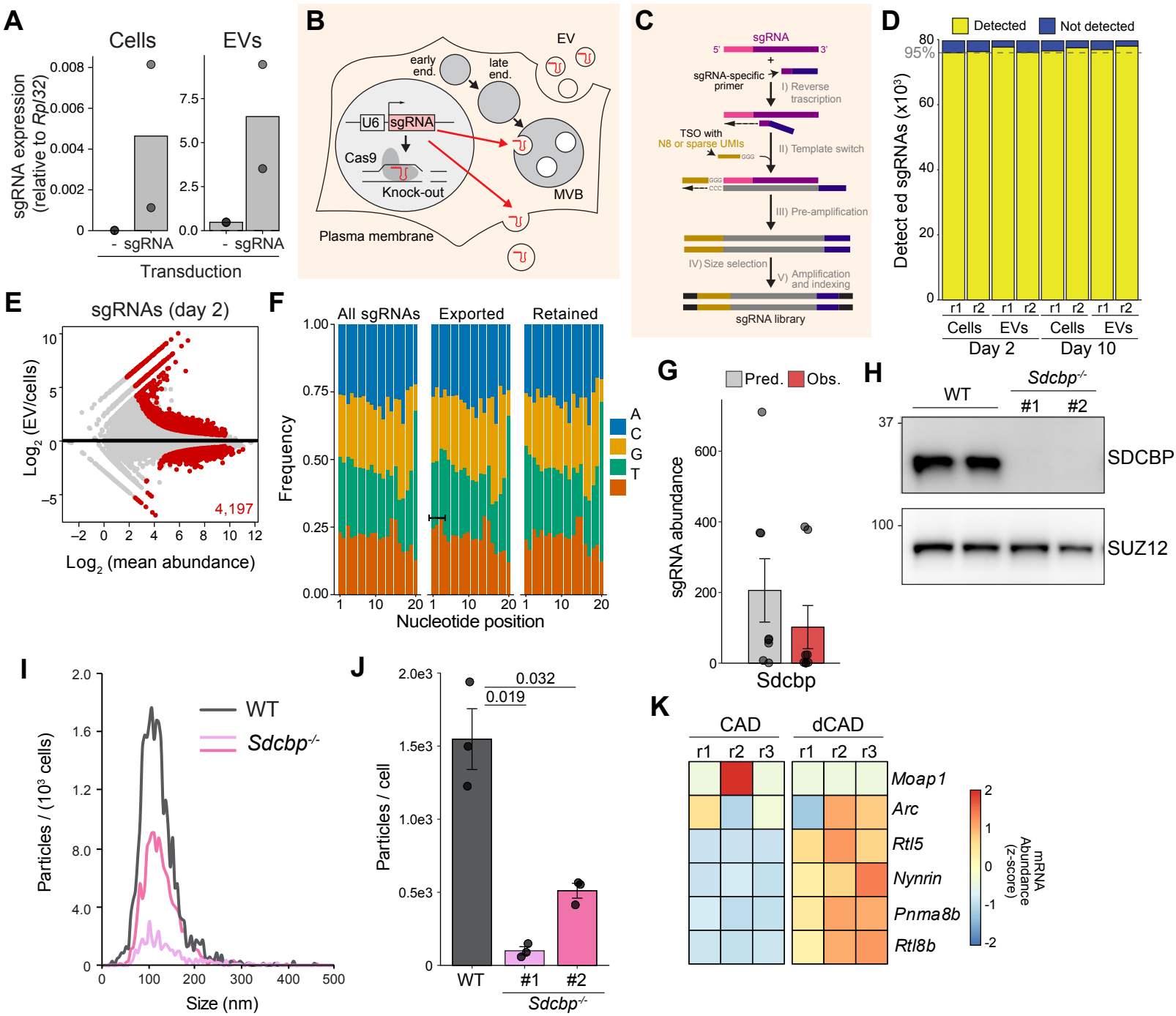

Figure S2. Analyses and validations on the genome-wide screen for exRNAs

(A) RT-qPCR for sgRNA abundance (expressed as ratio to Rpl32 RNA) in cells and EVs from sgRNA-expressing CAD and controls.

(B) Scheme of the logic underpinning the genome-wide screen. A fraction of sgRNAs expressed from a U6 promoter enter endogenous secretion pathways, for example by being loaded into intraluminal vesicles of multivesicular bodies (MVBs, derived from endosomal maturation) or directly by budding from the plasma membrane. This allows for the genotype of the originating cell to be determined via the sgRNA content of the EVs.

(C) Scheme of the LIDAR adaptation used to directly sequence the sgRNAs from the EVs.

(D) Number of sgRNAs that were detected (yellow) or not (blue) in cells and EV in each screen replicate. Individual samples are shown. Horizontal dashed line indicates the 95% of all sgRNAs included in the library.

(E) Comparison of the abundance of all individual sgRNAs inside cells vs. EVs at day 2 after transduction. Red, genes with significant difference (n = 2, adjusted p value < 0.1)

(F) Nucleotide representation at individual CRISPR RNA (crRNA) targeting sequence positions for all, preferentially exported, and preferentially retained sgRNAs. The bracket indicates the first 3 positions, enriched for Us in the exported sgRNAs.

(G) Average predicted (gray) and observed (red) values (SEM) for sgRNAs targeting Sdcbp. Circles represent values for the individual sgRNAs.

(H) Western blot for SDCBP and SUZ12 (control) in wild type and 2 different Sdcbp-/- CAD clones.

(I) Nanoparticle tracking analysis of EVs isolated from wild type and Sdcbp-/- CADs. The plot shows the number of particles normalized to the number of starting million cells [particles/(mL*million cells)] on the y axis and their size on the x axis.

(J) Average particles/(mL*million cells) (SEM), calculated as in (I), secreted by wild type and 2 different Sdcbp-/- CAD clones (n = 3). Individual replicates are shown.

(K) Z score-converted mRNA abundance (normalized DEseq2 counts) for the domesticated retroviral genes showed in Fig. 2F, before ("CAD") and after ("dCAD") CAD cell differentiation into a more mature neuronal form.

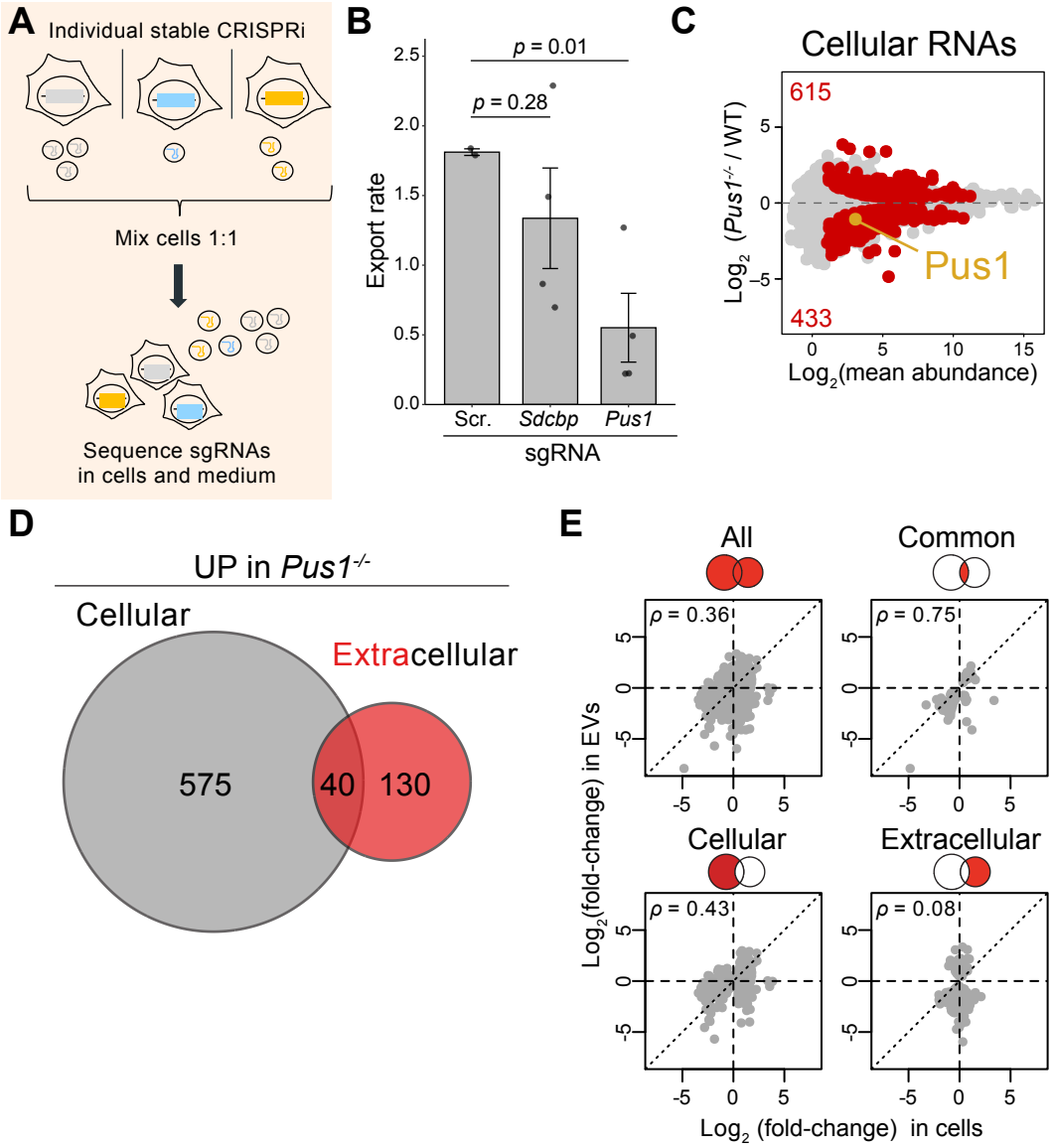

Figure S3. Validation of Pus1 and analyses on exRNAs from Pus1-/- cells

(A) Scheme of secondary CRISPRi screen. Stable CAD cells, transduced with different CRISPRi sgRNAs were mixed in equal numbers. Then, the abundance of sgRNAs in the pooled cells and in the tissue culture medium (extracellular) was measured by LIDAR.

(B) Export rate of the indicated CRISPRi sgRNAs, calculated as a ratio of extracellular over intercellular abundance. “Scr.” denotes sgRNA scrambled control. P values are from Student’s t tests.

(C) Differences in cellular RNA abundance between wild type and Pus1-/-, as measured by LIDAR. Red, transcripts showing significant difference (n ≥ 3, adjusted p value < 0.1).

(D) Overlap between RNAs more abundant (“UP”) in Pus1-/- cells compared to WT, either inside the cells (gray, “cellular”) or in EVs (red, “extracellular”).

(E) Correlations in the change in RNA abundance between wild type and Pus1-/- CADs (x axis) and EVs (y axis) for the RNAs significantly changed (adjusted p value < 0.1) in either set. Spearman’s correlation values are reported.

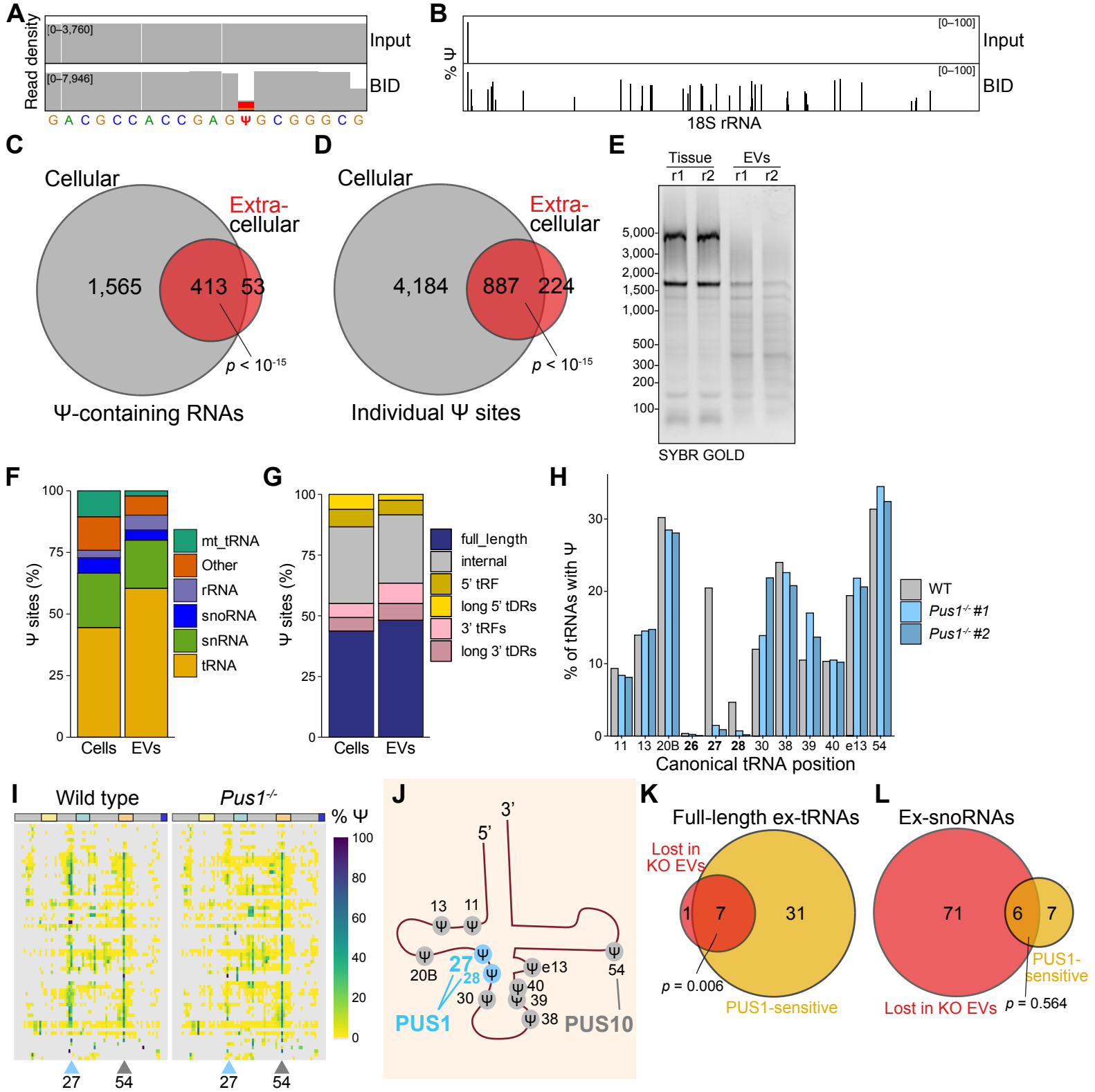

Figure S4. Validation of Ψ sequencing and analyses on exRNAs from Pus1-/- CADs

(A) LIDAR read densities (normalized to counts per millions) for individual nucleotides of an in vitro-transcribed Ψ-containing RNA. Top, input; bottom, BID-treated

(B) Inferred % of Ψ based on % of deletion in LIDAR reads mapping to 18s rRNA from CAD RNA. Top, input; bottom, BID-treated

(C–D) Overlap between Ψ-containing RNAs (C) or individual sites (D) identified in CADs and EVs. P values are from hypergeometric tests.

(E) Denaturing agarose-formaldehyde (2%) electrophoresis of total tissue (cellular) and EV RNA from cauda epididymis (individual replicates are shown).

(F) Distribution of transcripts containing PUS1-sensitive Ψ sites in CADs and EVs among the indicated RNA classes. Data from 2 biological replicates.

(G) Distribution of reads containing PUS1-sensitive Ψ sites and mapping to tRNAs genes among the indicated types of tRNA-derived species in cells and EVs.

(H) % of Ψ modification detected at each canonical tRNA position in wild type or Pus1-/- CAD EVs. Data from the two different Pus1-/- clones are shown separately.

(I) % of Ψ at every canonical tRNA position (column) for every tRNA iso-acceptor containing a U at position 27 (rows) in EVs from wild type (left) or Pus1-/- (right) CADs.

(J) Scheme of canonical Ψ sites on tRNAs. In blue, Ψ sites dependent on PUS1.

(K) Overlap between significantly reduced full-length tRNAs in Pus1-/- (red) and PUS1 full-length tRNA targets (yellow) in EVs. P value is from a hypergeometric test.

(L) Same as (K) but for snoRNAs.

For all panels data were from two biological replicates. In the case of Pus1-/- the two individual knockout clones were used as combined replicates (n = 2 per clone).

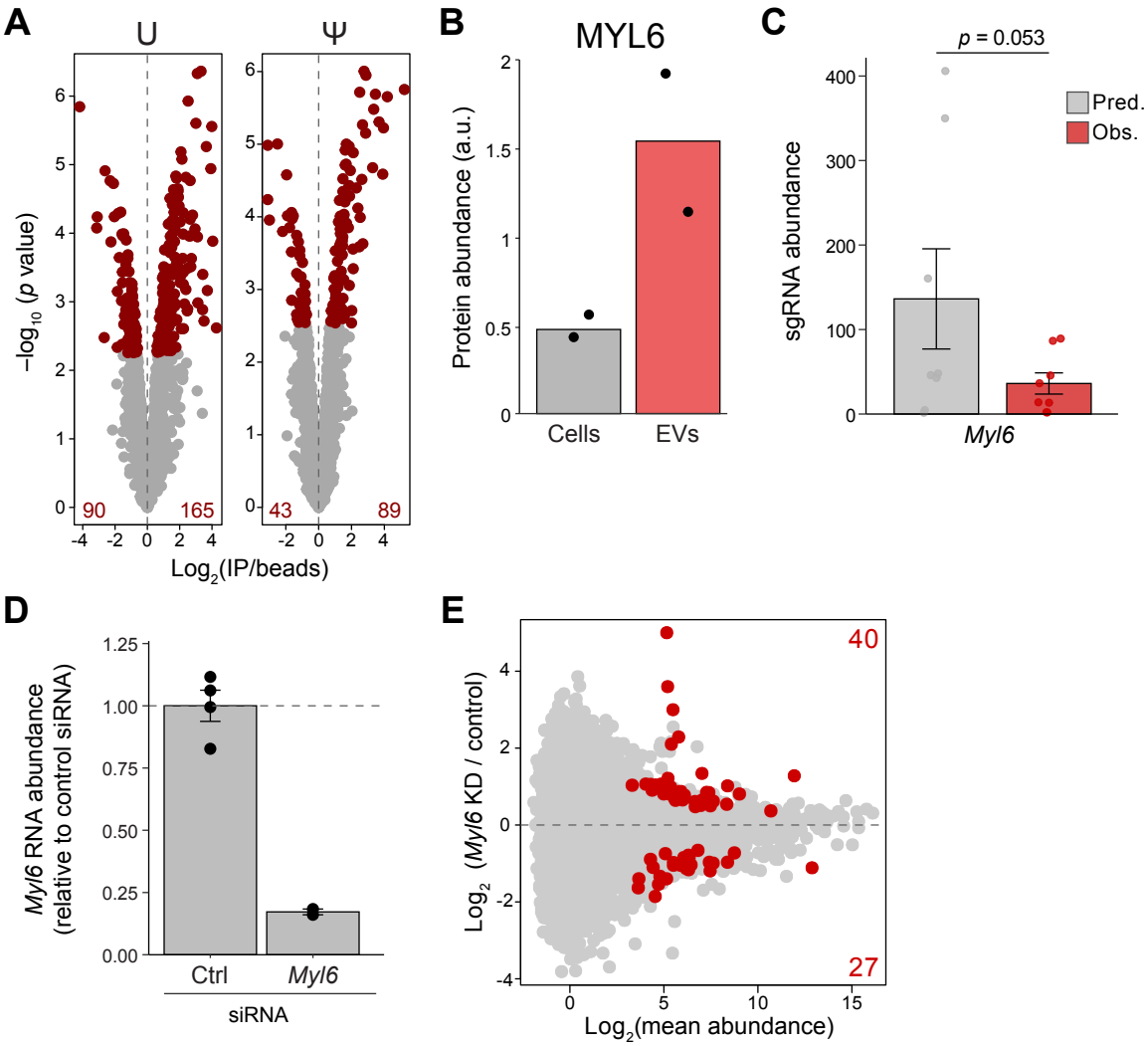

Figure S5. Additional analyses for MYL6

(A) IP/beads values for U- and Ψ-RNAs interactomes measured by mass spectrometry. In red, significantly different proteins (adjusted p < 0.1; n = 2).

(B) MYL6 protein abundance in CAD cells and EVs.

(C) Average predicted (gray) and observed (red) values (± SEM) for sgRNAs targeting Myl6. Circles represent individual sgRNAs. The p value reported is from the MaGECK analysis.

(D) Myl6 mRNA abundance relative to control (Rpl32). Bars show average SEM. Individual replicates are shown.

(E) Differences in intracellular RNA abundance between control and Myl6 knock down (KD) as measured by LIDAR. Red, transcripts showing significant difference (n ≥ 5, adjusted p value < 0.1).